One-Dimensional Fast Transient Simulator for Modeling CdS/CdTe Solar Cells

by

Da Guo

A Thesis Presented in Partial Fulfillment
of the Requirements for the Degree
Master of Science

Approved April 2013 by the
Graduate Supervisory Committee:

Dragica Vasileska, Chair
Igor Sankin
Stephen Goodnick

ARIZONA STATE UNIVERSITY

May 2013

ABSTRACT

Solar energy, including solar heating, solar architecture, solar thermal electricity and solar photovoltaics, is one of the primary alternative energy sources to fossil fuel. Being one of the most important techniques, significant research has been conducted in solar cell efficiency improvement. Simulation of various structures and materials of solar cells provides a deeper understanding of device operation and ways to improve their efficiency.

Over the last two decades, polycrystalline thin-film Cadmium-Sulfide and Cadmium-Telluride (CdS/CdTe) solar cells fabricated on glass substrates have been considered as one of the most promising candidate in the photovoltaic technologies, for their similar efficiency and low costs when compared to traditional silicon-based solar cells.

In this work a fast one dimensional time-dependent/steady-state drift-diffusion simulator, accelerated by adaptive non-uniform mesh and automatic time-step control, for modeling solar cells has been developed and has been used to simulate a CdS/CdTe solar cell. These models are used to reproduce transients of carrier transport in response to step-function signals of different bias and varied light intensity. The time-step control models are also used to help convergence in steady-state simulations where constrained material constants, such as carrier lifetimes in the order of nanosecond and carrier mobility in the order of $100 \text{ cm}^2/\text{Vs}$, must be applied.

Dedicated to Mom and the memory of Dad

ACKNOWLEDGMENTS

TABLE OF CONTENTS

LIST OF FIGURES

LIST OF TABLES

x

Chapter 1   INTRODUCTION

1.1.   Solar Energy

As the ultimate source of energy, the Sun shaped this blue planet called home. It generates atmospheric currents, drives river flow and provides energy in photo-synthesis, which converts solar energy directly into the chemical energy that fuels all living things on Earth. The annual amount of energy consumed by humans on Earth, roughly 5×10^{20} joules, can be delivered by the Sun in an hour. The enormous power supplied continuously by Sun, 1.2×10^5 terawatts, dwarfs every other energy source, renewable or fossil fuel. It dramatically exceeds the 13 TW power that human civilization produces[1].
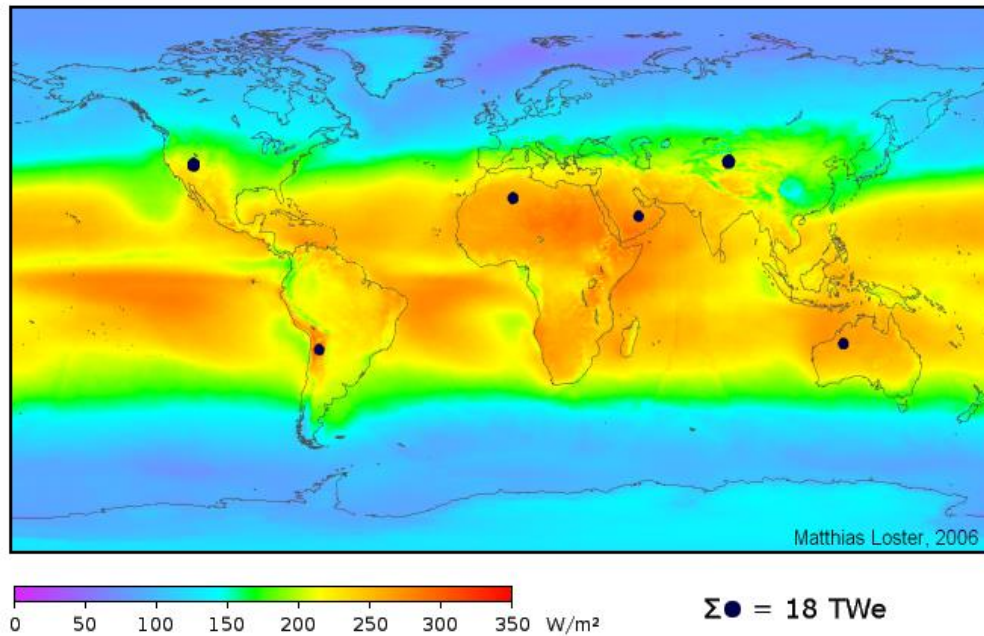
Figure 1.1   Average solar energy on Earth.

(Courtesy of Wikipedia)

As of today, solar energy technologies include solar heating and cooling, solar

1

thermal electricity and solar photovoltaics. Solar thermal technologies can be used for water heating, spacing heating, space cooling and process heat generation. Solar thermal electricity technology, also known as concentrated solar power systems, use mirrors and tracking systems to focus a large area of sunlight into a small beam, as illustrated below in Figure 1.2. The concentrated heat is then used as a source of a conventional power plant, where steam drives generators for electricity.
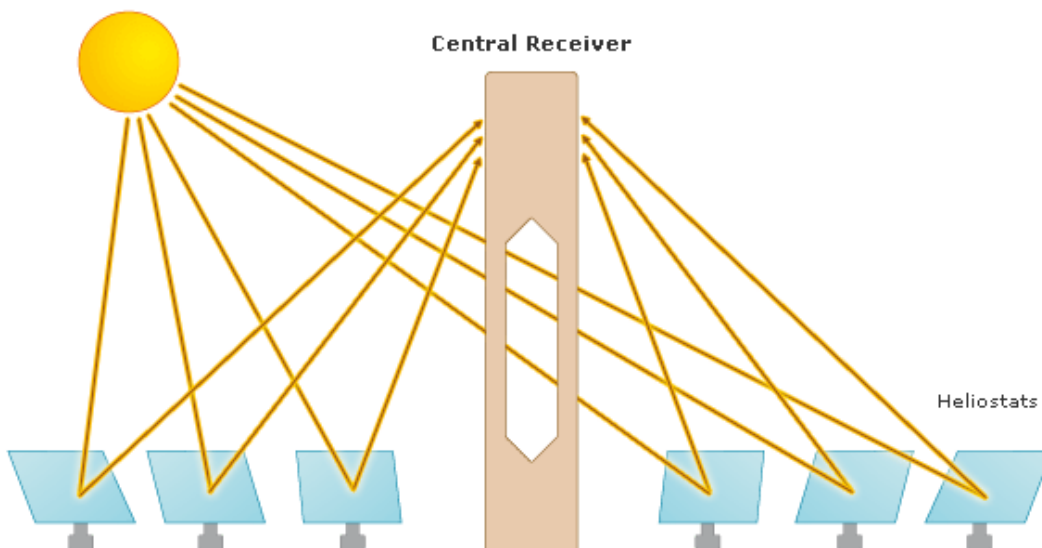
Figure 1.2   An illustration of Concentrated Solar Power Systems.

A photovoltaic cell, or solar cell, is a device that converts light into electric current directly by utilizing photoelectric effect. Although the history of solar cells can be dated back to 1880s, Pearson, Fuller and Chapin started the whole new chapter of photovoltaics by creating the first silicon solar cell in 1954[2].

1.2.   Solar Cell Operations

Solar cell works in three steps. First, Photons in sunlight are absorbed by solid

state materials, such as silicon and CdTe, known as photoelectric effect. Electron – hole pairs are generated with the absorption of photons. Secondly, carriers are separated by the built-in potential (or the depletion region) of pn junctions. At last, current flows when the separated carriers are extracted to external circuits. Figure 1.3 described these steps graphically.
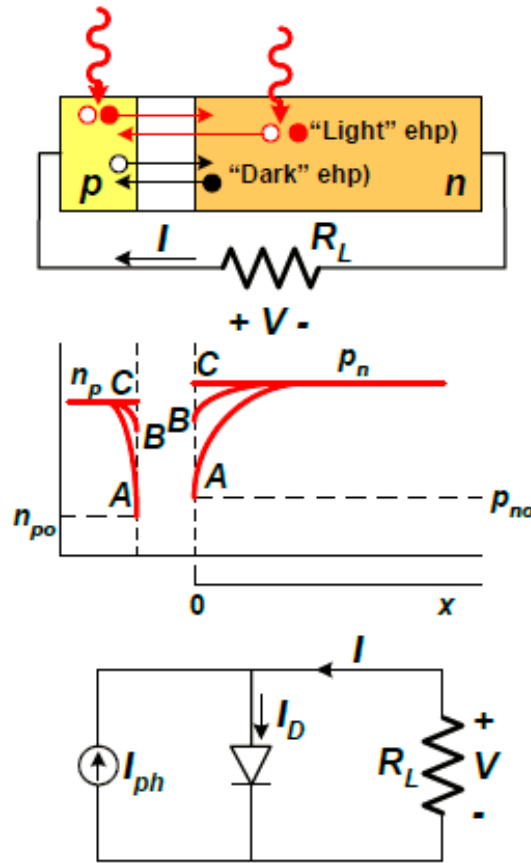
Figure 1.3 Three steps of the operation of solar cells.

The letter A, B and C in the middle of Figure 1.3, denote three operating conditions of solar cells. For condition A, where no bias or load is applied to the device, known as the ideal short circuit condition, carriers are being separated and extracted by

3

the pn junction itself. In this case, negative short circuit current, I_{sc} or J_{sc}, the largest operating current of a solar cell, can be produced. If we apply a certain forward bias, V_{oc}, to the diode that flat carrier densities are generated, Case C, the open circuit condition, can be achieved with zero current. Case C can also be interpreted as dark current balancing out the short circuit current. Theoretically, open circuit can be produced by applying an infinitely large load resulting in infinitesimally small current flowing. In reality, only a finite value of external load can be applied into the circuits. Thus the solar cell will operate between these two conditions, as shown by letter B in Figure 1.4, where positive bias applied and negative current flows, resulting in negative power consumption, which also means power is generated by the solar cell under illuminations.
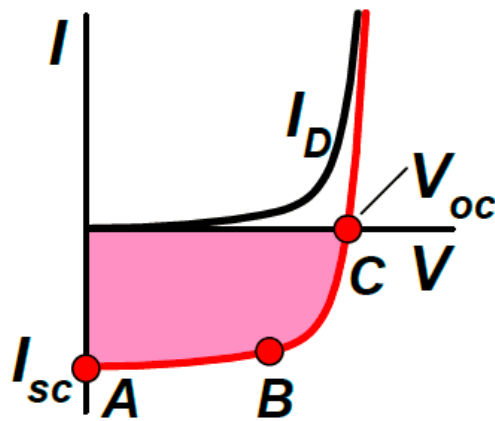
Figure 1.4   Typical IV characteristics of solar cells.

(Courtesy of Dr. Schroder)

The operating regime of solar cells is the range of bias, from 0 to V_{oc}, in which the cell generates power. The power reaches a maximum at the maximum power point, as marked 'P_{MAX}' in Figure 1.5. This occurs at a voltage V_{mp} with a corresponding current density J_{mp}, also shown below.

4
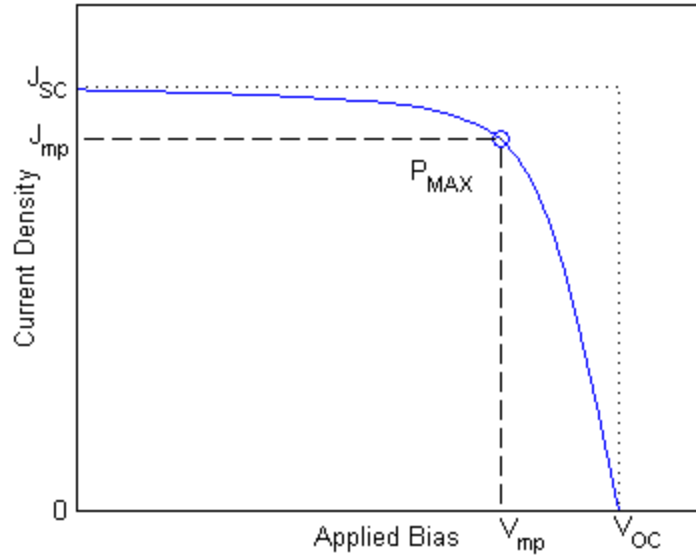
Figure 1.5   Simulated IV characteristics of solar cells.

The efficiency, η, one of the most important properties of solar cells, is the power density generated at the maximum power point as a fraction of the incident solar irradiance power density, P_s,

$$\eta = \frac{P_{MAX}}{P_s} = \frac{J_{mp}V_{mp}}{P_s} \qquad (1.1)$$

The efficiency is related to J_{sc} and V_{oc},

$$\eta = \frac{P_{MAX}}{P_s} = \frac{J_{sc}V_{oc} \cdot FF}{P_s} \qquad (1.2)$$

where *FF* is the fill factor, which describes the 'squareness' of the J-V characteristics, is defined as the ratio,

$$FF = \frac{J_{mp}V_{mp}}{J_{sc}V_{oc}} \qquad (1.3)$$

These four quantities: J_{sc}, V_{oc}, FF and η are the key performance characteristics of a solar cell. Typical numbers of these PV cell characteristics are shown below from Green[3].

Table 1.1   Performance of common PV cells.

Cell Type	Voc (V)	Jsc (mA/cm2)	FF	Efficiency (%)
crystalline Si	0.706	42.7	82.8	25.0
thin film GaAs	1.107	29.5	86.7	28.3
CIGS	0.713	34.8	79.2	19.6
CdTe	0.845	26.1	75.5	16.7

1.3. CdS/CdTe Solar Cells
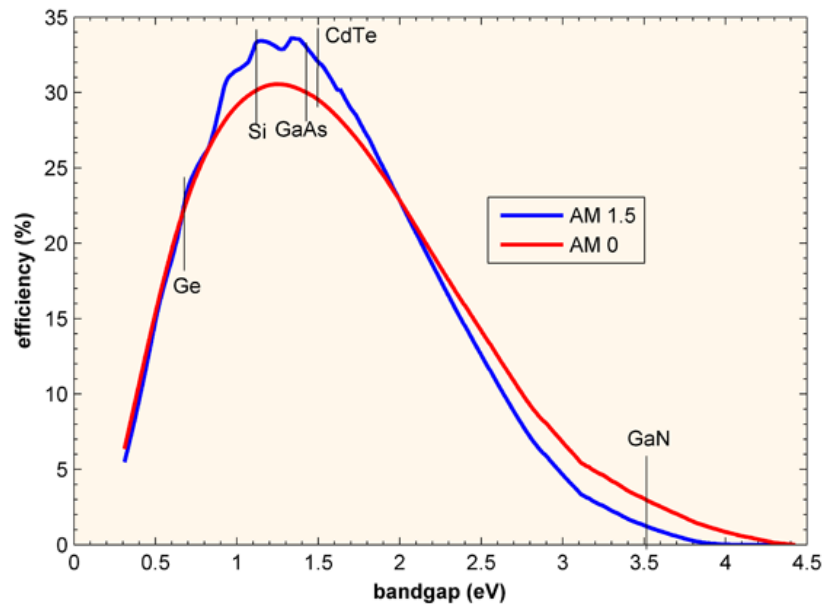
Figure 1.6   Detailed balance for AM0 and AM1.5.

As the most commercially successful thin film solar cell, cadmium telluride

(CdTe) has a market share of around 8% in the PV industry; this exceeds all other non-silicon solar cells. Research in CdTe dates back to the 1950s, after which the 1.5 eV bandgap of CdTe was found to be almost perfectly matched to the solar spectrum in terms of optimal conversion to electricity[4]. Figure 1.6 above shows the theoretical maximum efficiency one can get for different bandgaps. Another advantage of CdTe solar cells is the short optical absorption lengths. Two micrometer thick CdTe is able to absorb 99 percent of photons under AM1.5G solar illumination, while hundreds of microns of silicon is required.

Due to the poor quality of n-typed doping of CdTe, a simple heterojunction design evolved in early 1960s in which p-type CdTe was matched with n-type cadmium sulfide (CdS) as window layer. A thin CdS layer (less than a micron) developed in the 1990s by Chu[5, 6] and Britt[7] in order to allow more photons passing through, resulted in 15% efficiency, a great success in terms of commercial potential.

A transparent conducting oxide (TCO) layer was added to CdTe solar cells, to facilitate the movement of currents across the top of the cell as the cells were being scaled up in size for large area products called modules. In this simulator, tin oxide, the most popular TCO material, was employed. And we arrived at the standard configuration of CdTe solar cells, as depicted in Figure 1.7.

Many improvements have been developed during the last two decades for higher conversion efficiency of CdTe solar cells, such as better junction quality, longer carrier lifetime and new buffering layers in laboratories; these improvements have resulted in 18.3% conversion efficiency achievement by GE Global Research and NREL's

7

confirmation in 2012[8]. In the commercial productions, average module efficiency of 11.7% has been claimed by First Solar[9].

| n-SnO$_2$, 0.1 µm |
| n-CdS, 0.2 µm |
| p-CdTe, 3-5 µm |
| Metal Contact |
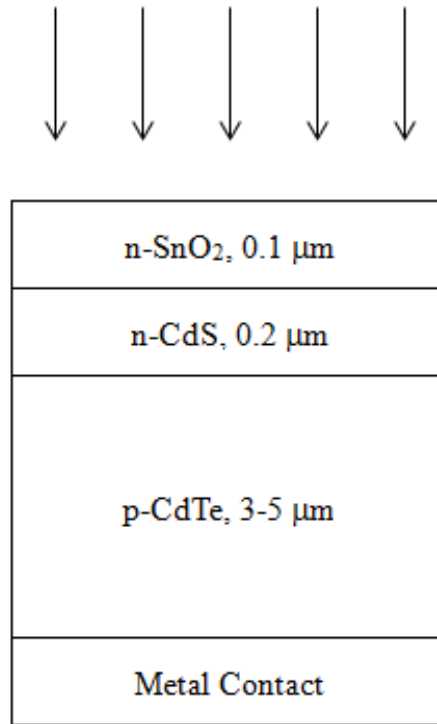
Figure 1.7   Typical configuration of a CdTe solar cell

1.4.   Semiconductor Device Simulations

Semiconductor device simulations provide an understanding of actual operations of solid state devices, with the necessary level of sophistication to capture the essential physics while at the same time minimizing the computational burden so that the results can be obtained within a reasonable time frame.

1.4.1. Importance of Simulation

Due to increasing costs for R&D and production facilities with shorter process

technology life cycles, device simulation tools have been developed tremendously within the semiconductor industry. Device modeling offers many advantages such as: providing problem diagnostics, providing full-field in-depth understanding, providing insight into extremely complex product sets where no direct characterization can be conducted, evaluating what-if scenarios rapidly, decreasing design cycle time and decreasing time to market. Simulations require enormous technical depth and expertise not only in simulation techniques and tools but also in the fields of physics and chemistry. Laboratory infrastructure and experimental expertise are essential for both model verification and input parameter evaluation in order to ensure truly effective and predictive simulations. The developer of simulation tools needs to be closely tied to the development activities in the research, the laboratories and commercial productions in industry.

1.4.2. General Device Simulation Framework
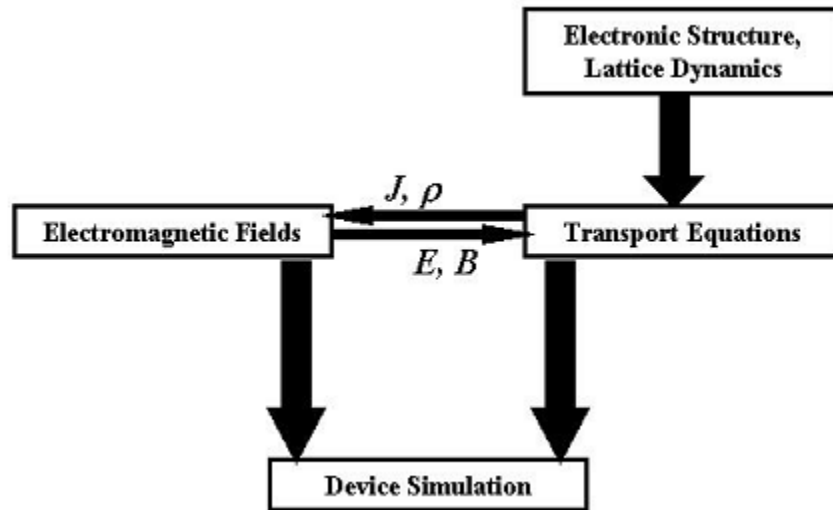
Figure 1.8   Schematic description of the device simulation sequence

(Courtesy of Dr. Vasileska & Dr. Goodnick)

Figure 1.8 shows the main components of semiconductor device simulations at any level. It begins with the electronic properties of solid state materials. The two main kernels, transport equations that govern charge flow and electromagnetic fields that drive charge flow, must be solved self-consistently and simultaneously with one and another, due to their strong coupling. The solution of transport equations, carrier distribution, can be used to evaluating the electromagnetic fields by solving Poisson's equation in the quasi-static approximation. Electric field profiles are essential to obtain current and carrier density profiles from the transport equations. Although advanced models such as hydrodynamic equations, Monte Carlo method and Green's Function method have been developed, drift diffusion equations were employed for the transport equations in this project, due to its simplicity for implementation, its relatively small computational burden and its accuracy for devices larger than 0.5 microns.

Implementation of the Poisson's equation, drift diffusion equations and their solution techniques will be discussed in the next chapter. We will introduce other physical models, such as generation/recombination mechanisms and metal contacts in Chapter 3. In Chapter 4, our simulator will be compared with the results from commercial software such as Atlas, Silvaco. Interesting results, especially the transient behaviors of CdTe solar cells, will also be analyzed in Chapter 4. Transient simulator is implemented because of two reasons: (a) to get more accurate steady-state results with regard to the current conservation; and (b) to study true transients in the device that allow one to extract minority carrier lifetimes, etc.

Finally, this dissertation work was performed to provide better and more flexible solver from what currently exists in the academia and industry in terms of TCAD.

Chapter 2   NUMERICAL METHODS

In this chapter, the discretized form of Poisson's equation and continuity equations will be derived for heterojunctions.

2.1.   Poisson Equation

Poisson's equation describes the relationship between electron charge and the electrostatic potentials[10]:

$$\nabla(\varepsilon(\nabla\phi)) = -q(p - n + N_D^+ - N_A^-) \tag{2.1}$$

where ϕ is the spatially varying electrostatic potential, ε is the permittivity, q is the fundamental charge, p is the hole density, n is electron density, N_D^+ is the ionized donor concentration and N_A^- is the activated acceptor concentration. In this simulator, instead of Boltzmann's statistics, Fermi-Dirac statistics are considered and the following equations are employed:

$$n = N_C F_{1/2}\left[\frac{E_F - E_C}{kT}\right]$$
$$p = N_V F_{1/2}\left[\frac{E_V - E_F}{kT}\right] \tag{2.2}$$

where N_C and N_V are the conduction and valence band effective density of states, E_F is the Fermi energy level, E_C is the conduction band energy level, E_V is the valence band energy level, k is the Boltzmann's constant, T is the lattice temperature and kT is the thermal energy in the system. Instead of solving the Fermi integral, a simple analytical approximation was employed to estimate the integral of the Fermi-Dirac distribution function[11].

2.1.1. Normalization of the Poisson's Equation

Under equilibrium conditions, with all parameters as given above, 1D Poisson's equation can be rewritten as equation 2.3:

$$\frac{d}{dx}(\varepsilon\frac{d\phi}{dx}) = -q(p-n+N_D^+ - N_A^-) \tag{2.3}$$

Now consider Boltzmann statistics here, n and p can be defined by the equations 2.4,

$$n = n_i \exp(\frac{\phi}{V_T})$$
$$p = n_i \exp(-\frac{\phi}{V_T}) \tag{2.4}$$

where n_i is the intrinsic carrier density. Assuming that $\phi = \phi + \delta$, applying $e^{\pm\delta} = 1 \pm \delta$ when δ is small, substituting this in equation 2.4 and using $(N_D^+ - N_A^-) / n_i = C$, equation 2.5 reads,

$$\frac{d}{dx}(\varepsilon\frac{d\phi}{dx}) = -qn_i(e^{-\frac{\phi}{V_T}} - e^{\frac{\phi}{V_T}} + C) + qn_i(e^{-\frac{\phi}{V_T}} + e^{\frac{\phi}{V_T}})\delta \tag{2.5}$$

Substituting $\delta = \varphi_{new} - \varphi_{old}$, we get

$$\frac{d}{dx}(\varepsilon\frac{d\phi^{new}}{dx}) - qn_i(e^{-\frac{\phi}{V_T}} + e^{\frac{\phi}{V_T}})\phi^{new} = -qn_i(e^{-\frac{\phi}{V_T}} - e^{\frac{\phi}{V_T}} + C) + qn_i(e^{-\frac{\phi}{V_T}} + e^{\frac{\phi}{V_T}})\phi^{old}$$

(2.6)

Rewriting in terms of n and p gives,

$$\frac{d}{dx}(\varepsilon\frac{d\phi^{new}}{dx}) - q(p+n)\phi^{new} = -q(p-n+Cn_i) + q(p+n)\phi^{old} \tag{2.7}$$

Changing permittivity to the relative permittivity, normalizing x with L_D, ϕ with V_T, p and

n with n_i, we will have the normalized form[12] of the Poisson's Equation:

$$\frac{d}{dx}(\varepsilon_r \frac{d\phi^{new}}{dx}) - (p+n)\phi^{new} = -(p-n+C) + (p+n)\phi^{old} \tag{2.8}$$

Although assumption of Boltzmann statistics has been made, the normalized Poisson's equation is suitable for Fermi-Dirac statistics[13].

2.1.2. Discretization of the Poisson's Equation

Using Selberherr's central difference scheme[14], $d\phi/dx$, $d^2\phi/dx^2$, $d\varepsilon_r/dx$ can written as following equation,

$$\frac{d\phi}{dx} = \frac{\phi_{i+1/2} - \phi_{i-1/2}}{\frac{1}{2}(dx_{i-1} + dx_i)}$$

$$\frac{d^2\phi}{dx^2} = \frac{\phi_{i+1} - \phi_i}{\frac{1}{2}(dx_{i-1} + dx_i)dx_i} - \frac{\phi_i - \phi_{i-1}}{\frac{1}{2}(dx_{i-1} + dx_i)dx_{i-1}} \tag{2.9}$$

$$\frac{d\varepsilon_r}{dx} = \frac{\varepsilon_{i+1} - 2\varepsilon_i + \varepsilon_{i-1}}{dx_{i-1} + dx_i}$$

Expanding Equation 2.8 with Equation 2.9, we get,

$$a_i\phi_{i-1}^{new} + b_i\phi_i^{new} + c_i\phi_{i+1}^{new} = f_i$$

$$a_i = (\frac{\varepsilon_{i-1} - \varepsilon_{i+1}}{dx_i + dx_{i-1}} - \frac{2\varepsilon_i}{dx_{i-1}})/(dx_i + dx_{i-1})$$

$$b_i = \frac{2\varepsilon_i}{dx_{i-1} \cdot dx_{i-1}} - p_i - n_i \tag{2.10}$$

$$c_i = (\frac{\varepsilon_{i+1} - \varepsilon_{i-1}}{dx_i + dx_{i-1}} - \frac{2\varepsilon_i}{dx_i})/(dx_i + dx_{i-1})$$

$$f_i = n_i - p_i - C_i - \phi_i^{old}(n_i + p_i)$$

where i represents the number of the grid point.

13

The finite difference discretization of the one-dimensional Poisson's equation leads to the coefficient matrix as the follows, with Dirichlet Boundary conditions (Ohmic Contact in this case) applied,

$$
\begin{pmatrix}
1 & 0 & & & & & & 0 \\
a_2 & b_2 & c_2 & & & & & \\
& a_3 & b_3 & c_3 & & & & \\
& & \ddots & \ddots & & & & \\
& & & a_{n-2} & b_{n-2} & c_{n-1} & & \\
& & & & a_{n-1} & b_{n-1} & c_{n-1} & \\
0 & & & & & 0 & 1
\end{pmatrix}
\begin{pmatrix}
\phi_1^{new} \\
\phi_2^{new} \\
\vdots \\
\vdots \\
\vdots \\
\phi_{n-1}^{new} \\
\phi_n^{new}
\end{pmatrix}
=
\begin{pmatrix}
f_1 \\
f_2 \\
\vdots \\
\vdots \\
\vdots \\
f_{n-1} \\
f_n
\end{pmatrix}
\tag{2.11}
$$

The solution technique of this coefficient matrix will be discussed in section 2.6.

2.2. Discretization of Continuity Equations

To discretize the continuity equations, the determination of the currents on the mid-point of each neighboring grid points is required. Since all data are accessible only at the grid nodes, interpolation schemes must be employed. In consistency with Poisson's equation we discussed, it is a common assumption that the potential varies linearly between connecting points; this is based on another assumption that constant field is observed between neighboring nodes. In addition, interpolation of carrier densities at the mid-points is also necessary to calculate the current. One simple way to evaluate the carrier density is to take the arithmetic average between two nodes under the assumption of linear variation of carrier densities. However, the exponential relationships between carrier density and electrostatic potentials make the linear variation valid only at small potential difference and near zero electric field between nodes, which is not acceptable

14

for non-equilibrium device simulation.

An optional approach is provided by Scharfetter and Gummel to solve this problem[15] with the acceptable linear potential variation between neighboring mesh nodes. Consider the one-dimensional electron current continuity equation:

$$\frac{\partial n}{\partial t} = \frac{1}{q}\nabla \cdot J_n - U \tag{2.12}$$

which, by using the half-point difference gives:

$$\frac{\partial n}{\partial t} = \frac{1}{q}\frac{J^n_{i+1/2} - J^n_{i-1/2}}{(dx_{i-1}+dx_i)/2} - U_i \tag{2.13}$$

where Drift Diffusion model is being employed and we have,

$$J^n_{i+1/2} = qn\mu^n_{i+1/2}E_{i+1/2} + qD^n_{i+1/2}\frac{dn}{dx} \tag{2.14}$$

where μ is the carrier mobility, E is electric field strength and D is the diffusion coefficients. Equation 2.14 can be written as:

$$\frac{dn}{dx} = \frac{\mu^n_{i+1/2}}{D^n_{i+1/2}}nE_{i+1/2} + \frac{J^n_{i+1/2}}{qD^n_{i+1/2}} \tag{2.15}$$

Knowing that $D=\mu V_T$ and $E_{i+1/2}=(\phi_{i+1}-\phi_i)/dx_i$, one arrives at,

$$\frac{dn}{dx} - n\frac{1}{V_T}\frac{\phi_{i+1}-\phi_i}{dx_i} = \frac{J^n_{i+1/2}}{qD^n_{i+1/2}} \tag{2.16}$$

interpreted by the following equation,

$$\frac{dn}{dx} = \frac{dn}{d\phi}\frac{d\phi}{dx} = \frac{\phi_{i+1}-\phi_i}{dx_i}\frac{dn}{d\phi} \tag{2.17}$$

Equation 2.17 is next summarized as:

$$\frac{dn}{d\phi} - \frac{n}{V_T} = \frac{dx_i}{\phi_{i+1} - \phi_i} \frac{J^n_{i+1/2}}{qD^n_{i+1/2}} \tag{2.18}$$

Using Laplace transformation, we get:

$$n(\phi) = n_i \left(1 - g(\phi)\right) + n_{i+1} g(\phi) \tag{2.19}$$

where $g(\phi)$ is known as the growth function. Therefore, the Drift-Diffusion model electron current can be written as:

$$J^n_{i+1/2} = \frac{qD^n_{i+1/2}}{dx_i} \left(n_{i+1} B\left(\frac{\phi_{i+1} - \phi_i}{V_T}\right) - n_i B\left(\frac{\phi_i - \phi_{i+1}}{V_T}\right) \right) \tag{2.20}$$

Similarly,

$$J^n_{i-1/2} = \frac{qD^n_{i-1/2}}{dx_{i-1}} \left(n_i B\left(\frac{\phi_i - \phi_{i-1}}{V_T}\right) - n_{i-1} B\left(\frac{\phi_{i-1} - \phi_i}{V_T}\right) \right) \tag{2.21}$$

where B is the Bernoulli function,

$$B(x) = \begin{cases} -x, & x \le x_1 \\ \dfrac{x}{e^x - 1}, & x_1 < x < x_2 \\ 1 - \dfrac{x}{2}, & x_2 \le x \le x_3 \\ \dfrac{xe^{-x}}{1 - e^{-x}}, & x_3 < x < x_4 \\ xe^{-x}, & x_4 \le x < x_5 \\ 0, & x \ge x_5 \end{cases} \tag{2.22}$$

Substituting Equation 2.20 and 2.21 into Equation 2.14, with implicit Euler method applied for the time discretization [16], gives the discretized electron continuity equation:

$$an_i \cdot n_{i-1}^{new} + bn_i \cdot n_i^{new} + cn_i \cdot n_{i+1}^{new} = fn_i$$

$$an_i = \frac{2 \cdot D_{i-1/2}^n}{dx_{i-1}(dx_i + dx_{i-1})} B(\frac{\phi_{i-1} - \phi_i}{V_T})$$

$$bn_i = -\frac{2}{dx_i + dx_{i-1}} (\frac{D_{i-1/2}^n}{dx_{i-1}} B(\frac{\phi_i - \phi_{i-1}}{V_T}) + \frac{D_{i+1/2}^n}{dx_i} B(\frac{\phi_i - \phi_{i+1}}{V_T})) + \frac{1}{\Delta t} \qquad (2.23)$$

$$cn_i = \frac{2 \cdot D_{i+1/2}^n}{dx_i(dx_i + dx_{i-1})} B(\frac{\phi_{i+1} - \phi_i}{V_T})$$

$$fn_i = U_i - \frac{n_i^{old}}{\Delta t}$$

where U_i is the net generation rate of carriers, Δt is the time step interval, and

$$D_{i-1/2}^n = V_T \cdot \mu_{i-1/2}^n = V_T \cdot \frac{\mu_{i-1}^n + \mu_i^n}{2}$$

$$D_{i+1/2}^n = V_T \cdot \mu_{i+1/2}^n = V_T \cdot \frac{\mu_i^n + \mu_{i+1}^n}{2} \qquad (2.24)$$

Similarly, discretized continuity equation of hole is derived to give

$$ap_i \cdot p_{i-1}^{new} + bp_i \cdot p_i^{new} + cp_i \cdot p_{i+1}^{new} = fp_i$$

$$ap_i = \frac{2 \cdot D_{i-1/2}^P}{dx_{i-1}(dx_i + dx_{i-1})} B(\frac{\phi_i - \phi_{i-1}}{V_T})$$

$$bp_i = -\frac{2}{dx_i + dx_{i-1}} (\frac{D_{i-1/2}^P}{dx_{i-1}} B(\frac{\phi_{i-1} - \phi_i}{V_T}) + \frac{D_{i+1/2}^P}{dx_i} B(\frac{\phi_{i+1} - \phi_i}{V_T})) + \frac{1}{\Delta t} \qquad (2.25)$$

$$cp_i = \frac{2 \cdot D_{i+1/2}^P}{dx_i(dx_i + dx_{i-1})} B(\frac{\phi_i - \phi_{i+1}}{V_T})$$

$$fp_i = U_i - \frac{p_i^{old}}{\Delta t}$$

The calculation of time step interval will be discussed in section 2.5, while the physical models implemented for the net generation rate will be evaluated in section 3.1. Equations 2.23 and 2.25, with appropriate boundary conditions applied, which will be

17

discussed in section 3.2, can be solved iteratively[17] as described in section 2.6.

2.3.   Incorporation with Heterojunctions

We have already discussed the discretization of Poisson's equation and continuity equation for homojunctions in section 2.1 and 2.2. For heterostructures, modifications must be made to the electrostatic potential in order to adjust band offsets between different materials. Otherwise, abrupt electrostatic potential leads to divergence in the iterative solver. In this project, *Band Parameter Approach*[18] is employed to take into account the different band parameters, including bandgaps and electron affinities, to ensure ϕ varies continuously along the heterojunctions.
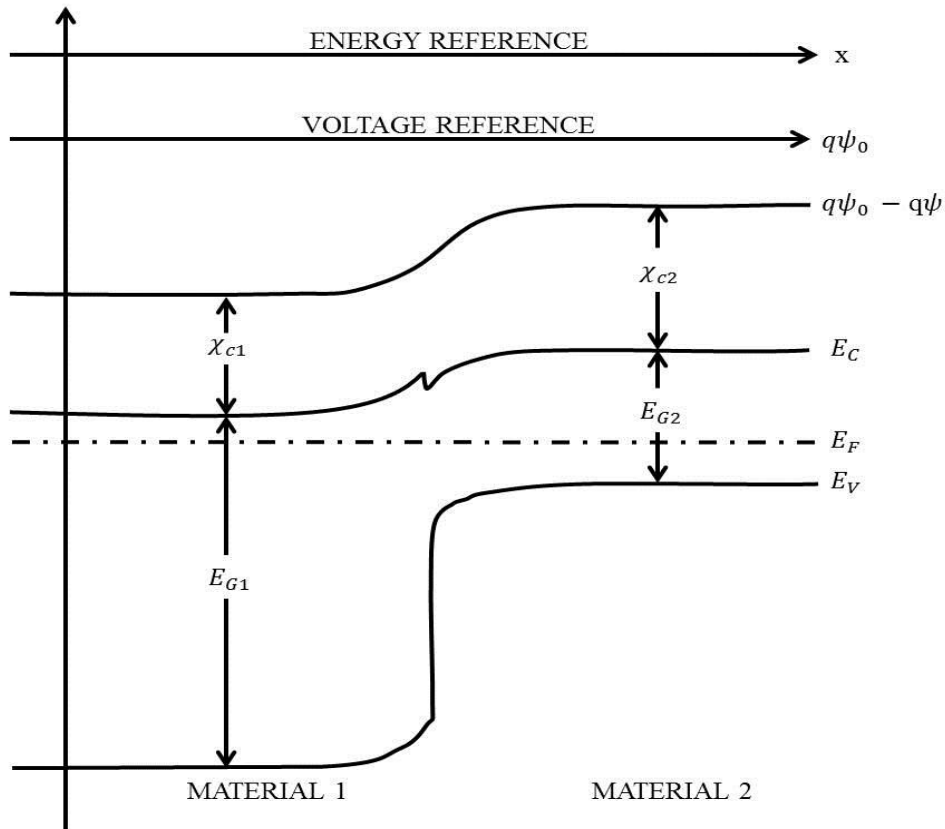
Figure 2.1   Equilibrium energy band diagram of an abrupt heterostructure.

18

With the aid of Figure 2.1, which shows us a band diagram of heterostructure comprising of two materials, we can have a better understanding of this band parameter approach. Let's begin with the conduction band and the valence band,

$$E_C = q\psi_0 - q\psi - \chi_C$$
$$E_V = q\psi_0 - q\psi - \chi_C - E_G$$

(2.26)

As stated before, the carrier concentration should be written as:

$$n = N_C \exp\left[(E_{Fn} - E_C)/K_B T\right]$$
$$p = N_V \exp\left[(E_V - E_{Fp})/K_B T\right]$$

(2.27)

Equation 2.27 can also be expressed as:

$$n = N_C \exp\left[\frac{q}{K_B T}\left(-\phi_n - \psi_0 + \psi + \frac{\chi_C}{q}\right)\right]$$

$$p = N_V \exp\left[\frac{q}{K_B T}\left(\psi_0 - \psi - \frac{\chi_C}{q} - \frac{E_G}{q} + \phi_p\right)\right]$$

(2.28)

Also we have,

$$N_C = n_{i2} \exp\left[\ln\left(\frac{N_C}{n_{i2}}\right)\right]$$

$$N_V = n_{i2} \exp\left[\ln\left(\frac{N_V}{n_{i2}}\right)\right]$$

(2.29)

substituting Equation 2.29 into 2.28,

$$n = n_{i2} \exp\left[\frac{q}{K_B T}\left(\psi - \phi_n - \psi_0 + \frac{\chi_C}{q} + \frac{K_B T}{q}\ln\frac{N_C}{n_{i2}}\right)\right]$$

$$p = n_{i2} \exp\left[\frac{q}{K_B T}\left(\psi_0 - \psi - \frac{\chi_C}{q} - \frac{E_G}{q} + \phi_p + \frac{K_B T}{q}\ln\frac{N_V}{n_{i2}}\right)\right]$$

(2.30)

Next we choose material 2, which most likely will be CdTe in CdS/CdTe solar cells, as

the reference point, hence we could assume the band parameters to be zero for this material:

$$\theta_n = \frac{\chi_C}{q} - \psi_0 + \frac{K_B T}{q} \ln \frac{N_C}{n_{i2}} = 0$$

$$\theta_p = \psi_0 - \frac{\chi_C}{q} - \frac{E_G}{q} + \frac{K_B T}{q} \ln \frac{N_V}{n_{i2}} = 0$$

(2.31)

ψ_0 can be solved as:

$$\psi_0 = \frac{\chi_{C2}}{q} + \frac{K_B T}{q} \ln \frac{N_{C2}}{n_{i2}} = \frac{\chi_{C2}}{q} + \frac{E_G}{q} - \frac{K_B T}{q} \ln \frac{N_{V2}}{n_{i2}}$$

$$\psi_0 = \frac{\chi_{C2}}{q} + \frac{K_B T}{q} \ln \frac{N_{C2}}{n_{i2}} = \frac{\chi_{C2}}{q} + \frac{E_G}{q} - \frac{K_B T}{q} \ln \frac{N_{V2}}{n_{i2}}$$

(2.32)

where subscript '2', refers to material 2. And the band parameter of material 1 can now be written as:

$$\theta_n = \frac{\chi_C - \chi_{C2}}{q} + \frac{K_B T}{q} \ln \frac{N_C}{N_{C2}}$$

$$\theta_p = \frac{\chi_{C2} - \chi_C}{q} + \frac{E_{g2} - E_g}{q} + \frac{K_B T}{q} \ln \frac{N_V}{N_{V2}}$$

(2.33)

Equation 2.33 gives the band parameters consistent with the Boltzmann statistics. The band parameters for Fermi – Dirac Statistics had been derived by Lundstrom[19] as the following:

$$\theta_p = -(\chi(x) - \chi_r) - (E_G(x) - E_{Gr}) + \frac{kT}{q}\left(\frac{N_V(x)}{N_{Vr}}\right) + \frac{kT}{q}\log\left(\frac{f_{1/2}(\eta_V)}{e^{\eta_V}}\right)$$

$$\theta_n = (\chi(x) - \chi_r) + \frac{kT}{q}\log\left(\frac{N_C(x)}{N_{Cr}}\right) + \frac{kT}{q}\log\left(\frac{f_{1/2}(\eta_C)}{e^{\eta_C}}\right)$$

(2.34)

20

2.3.1 Poisson's Equation for Heterojunctions

We already discussed in section 2.1 the discretized Poisson's equation for homojunctions with permittivity varied. For complete heteroscturctures, except band parameters for adjusting quasi – Fermi level and carrier density, additional work is required to make the electrostatic potential to denote the relative energy level. Another band parameter, intrinsic level offset, which represents the difference between intrinsic levels of different materials, has been employed as below:

$$\theta_{offsets} = \frac{\chi_{C2} - \chi_C}{q} + \frac{1}{2}\frac{E_{g2} - E_g}{q} \tag{2.35}$$

By deducting these offsets before evaluating Equation 2.12, ϕ can be varied smoothly in an abrupt heterojunction. Also we need to restore the real electrostatic potentials by adding these offsets back when convergence is achieved for band structures plotting.

2.3.2 Continuity Equations for Heterojunctions

In section 2.2 we have derived the discretized continuity equation for non-uniform meshed homojunctions. Similar procedures will be conducted for the heterojunction equations, with appearance of new terms. Recall that the Drift – Diffusion current equation is of the form,

$$J_n = qn\mu_n E + qD_n \frac{dn}{dx} \tag{2.36}$$

Where the electric field strength, E, should be based on the Fermi level, as below:

$$\frac{dE_{Fn}}{dx} = \frac{dE_C}{dx} + \frac{K_B T}{q}\left[\frac{1}{n}\frac{dn}{dx} - \frac{dN_C}{dx}\right] \tag{2.37}$$

Equation 2.37 can be expanded as,

$$\frac{dE_{Fn}}{dx} = qE - \frac{d\chi_C}{dx} + \frac{K_B T}{n}\frac{dn}{dx} - \frac{K_B T}{N_C}\frac{dN_C}{dx} \qquad (2.38)$$

Combining Equation 2.36 and 2.38, the tradition drift diffusion terms and the effect of spatially varied electron affinity and density of states can be both reserved in Equation 2.39:

$$J_n = -qn\mu_n \frac{d}{dx}(\psi + \theta_n) + K_B T \mu_n \frac{dn}{dx}$$
$$J_p = -qn\mu_p \frac{d}{dx}(\psi - \theta_p) - K_B T \mu_p \frac{dp}{dx} \qquad (2.39)$$

Similarly as described in section 2.2, employing the Scharfetter and Gummel scheme after inserting Equation 2.39 into Continuity Equations, we obtain Equation 2.40 and 2.41. Note that $\phi^n = \phi + \theta_n$ for electrons.

$$an_i \cdot n_{i-1}^{new} + bn_i \cdot n_i^{new} + cn_i \cdot n_{i+1}^{new} = fn_i$$
$$an_i = \frac{2 \cdot D_{i-1/2}^n}{dx_{i-1}(dx_i + dx_{i-1})} B(\frac{\phi_{i-1}^n - \phi_i^n}{V_T})$$
$$bn_i = -\frac{2}{dx_i + dx_{i-1}}(\frac{D_{i-1/2}^n}{dx_{i-1}} B(\frac{\phi_i^n - \phi_{i-1}^n}{V_T}) + \frac{D_{i+1/2}^n}{dx_i} B(\frac{\phi_i^n - \phi_{i+1}^n}{V_T})) + \frac{1}{\Delta t} \qquad (2.40)$$
$$cn_i = \frac{2 \cdot D_{i+1/2}^n}{dx_i(dx_i + dx_{i-1})} B(\frac{\phi_{i+1}^n - \phi_i^n}{V_T})$$
$$fn_i = U_i - \frac{n_i^{old}}{\Delta t}$$

And $\phi^p = \phi - \theta_p$ for holes,

22

$$ap_i \cdot p_{i-1}^{new} + bp_i \cdot p_i^{new} + cp_i \cdot p_{i+1}^{new} = fp_i$$

$$ap_i = \frac{2 \cdot D_{i-1/2}^P}{dx_{i-1}(dx_i + dx_{i-1})} B(\frac{\phi_i^P - \phi_{i-1}^P}{V_T})$$

$$bp_i = -\frac{2}{dx_i + dx_{i-1}}(\frac{D_{i-1/2}^P}{dx_{i-1}} B(\frac{\phi_{i-1}^P - \phi_i^P}{V_T}) + \frac{D_{i+1/2}^P}{dx_i} B(\frac{\phi_{i+1}^P - \phi_i^P}{V_T})) + \frac{1}{\Delta t} \qquad (2.41)$$

$$cp_i = \frac{2 \cdot D_{i+1/2}^P}{dx_i(dx_i + dx_{i-1})} B(\frac{\phi_i^P - \phi_{i+1}^P}{V_T})$$

$$fp_i = U_i - \frac{p_i^{old}}{\Delta t}$$

2.4. Non-Uniform Mesh

Less grid points would accelerate the simulations, simply by lowering the number of calculations. It also means less accuracy, especially in heterojunctions, where crucial electrostatic potential and electric field exist. Non-uniform mesh is employed in this solver to relax the grid spacing where low electric field is observed and to retain dense meshing at junctions for high accuracy. In this section, the generation mechanism of non-uniform mesh will be introduced.

Initially a uniform mesh (*mesh1*) based on the Debye length criterion is generated and the equilibrium potential and electric field profiles (*efield1*) are solved iteratively, as will be discussed in section 2.7. Then, the mesh refinement (generation of non-uniform mesh) was done based on the uniform mesh electric field profile under equilibrium condition. The meshing factor was calculated using:

$$mesh2 = fh \cdot \log_{10}(|efield1| + 1) + fl \qquad (2.42)$$

where *efield1* is the uniform mesh electric field under equilibrium in unit of V/m, *fh* is the

meshing coefficient for high field part (which also represents depletion region), and fl is the tuning factor for low field region. As shown below (Figure 2.2), larger fh gives higher meshing factor for high electric field while smaller fl gives lower factor for low field. In order to avoid negative numbers in taking the log function, absolute value of the electric field plus one is employed.
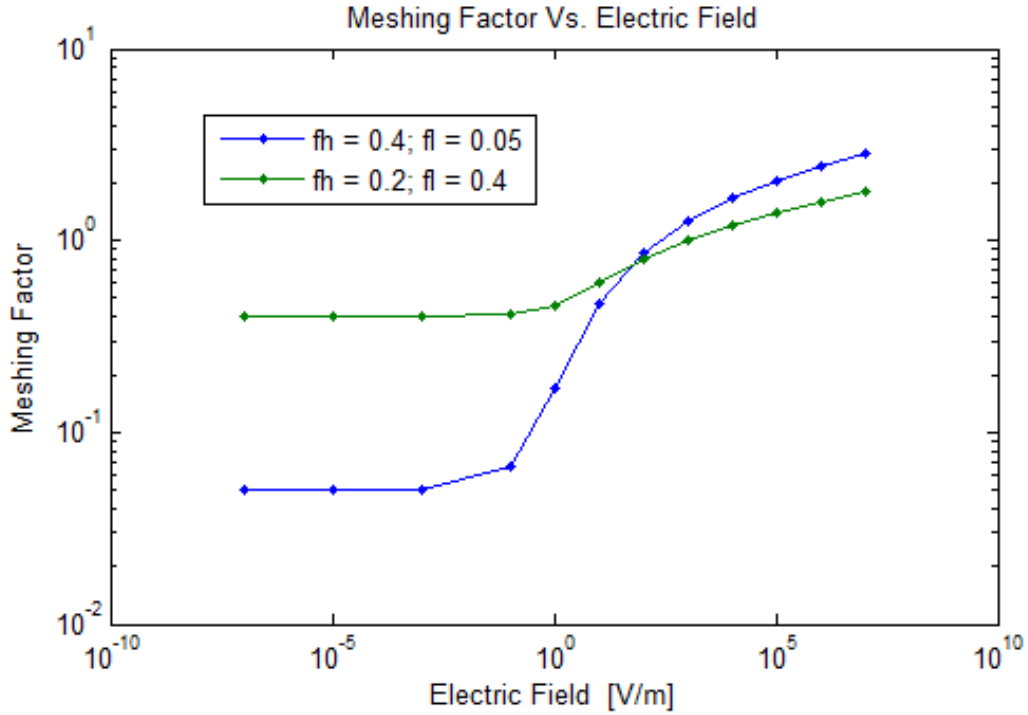
Figure 2.2   Meshing factor vs. Electric field.

Once the meshing factor profile is evaluated, the grid spacing is determined by local Debye Length and the meshing factor together,

$$dx = L_D / mesh2 \tag{2.43}$$

It is clear from the results presented in Figure 2.2 that the factors are higher than 1 for high electric field, which will guarantee the accuracy of this meshing strategy by meeting the general meshing criteria of grid spacing smaller than the Debye Length[20].

Since abrupt grid spacing would introduce spikes on the electrostatic potential profiles, keeping *dx* continuous is important for accurate simulations. The simple approach is to use one single Debye length for the entire meshing, which is convenient but not efficient. Employing the smallest Debye lengths from different materials leads to huge number of grid points, while using the largest will cause inappropriately coarse mesh and poor accuracy.
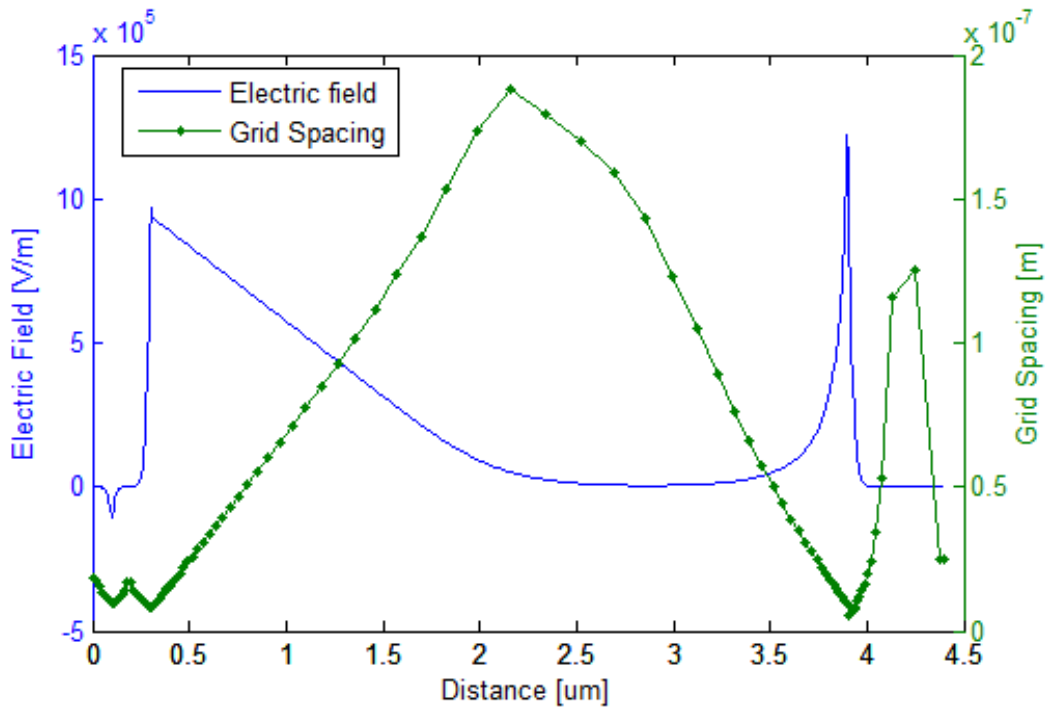
Figure 2.3   Grid spacing for a typical SnO/CdS/CdTe/ZnTe solar cell.

A more complicated approach is being implemented in this solver to ensure *dx* varies smoothly at the junctions. We determined the local Debye length on its relative position and the L_D of neighboring layer materials. As in the first half of CdTe layer in a typical SnO/CdS/CdTe/ZnTe solar cell, the local Debye length was evaluated by its own L_D, L_D of neighboring CdS layer and the relative position towards the CdS/CdTe heterojunction. While in the second half, the local Debye length should be calculated by

the Debye lengths of CdTe, neighboring ZnTe and the relative position towards the CdTe/ZnTe junction. Similar procedure was applied for the entire device, resulting in a meshing as depicted in the Figure 2.3 above, where comparison between electric field strength and grid spacing has been made. The smooth variation of *dx* has also been observed clearly.

2.5.   Automatic Time Step Control

Similarly to the idea of non-uniform mesh, automatic time step control was developed for this solver, in order to accelerate the transient simulations. The general mechanism is to make time steps larger when the current changes with respect to time are smaller and to make time steps smaller when current changes significantly. To ensure that the solver converges, we introduced *dt1* and *dt3* as convergence protection in this simulator.

The time step used at the beginning and end of a pulse signal, in our case *dt1*, should be small so that the solver could converge. If the time step is too small, extra useless computations will be conducted. Thus *dt1* must be determined by the pulse width and limited by 10ps; the result is a semi-empirical number which can assure convergence for most cases:

$$\frac{1}{dt1} = \frac{1}{10^{-11}} + \frac{100}{pulse\_width} \tag{2.44}$$

Figure below shows the *dt1* for variety of pulse widths from 1us to 1ps. It is clear that if we make dt1 as the constant time step in this solver, 100,000 iterations will be conducted for a 1us pulse, regardless of an even longer time period of current or

26

Photocurrent decay.
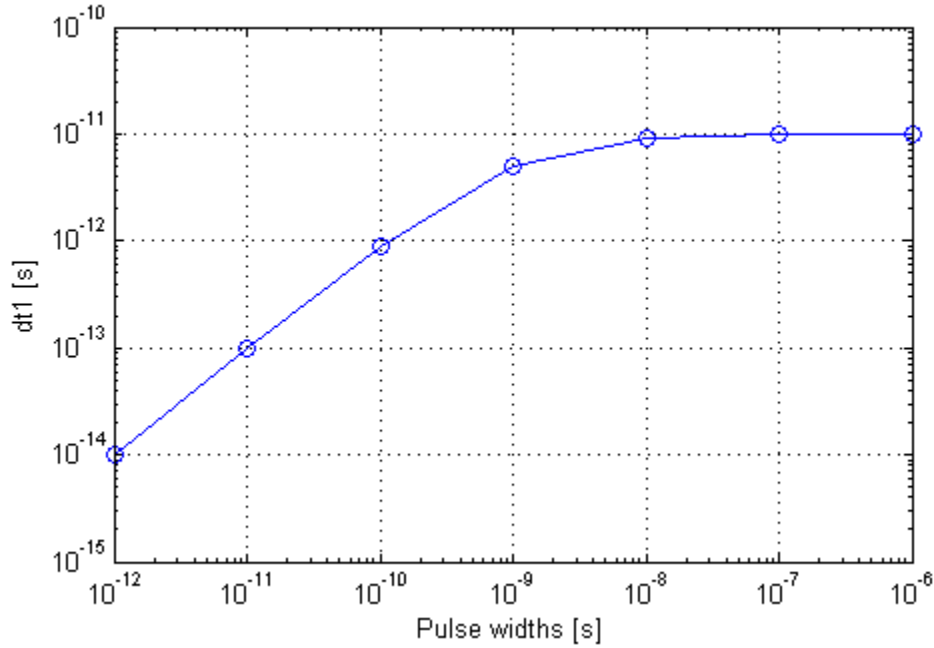
Figure 2.4   *dt1* vs. pulse widths.

As mentioned above, *dt1* will be used at the beginning and end of pulse signals where significant current changes can be predicted. Thus *dt3*, the timing of the activation of automatic time step control, is crucial to this solver. Similarly to *dt1*, *dt3* was evaluated by one tenth of the pulse widths and a semi-empirical 10ns time interval within which 90% of current changes can be finished, as the following equation describes:

$$\frac{1}{dt3} = \frac{1}{10^{-8}} + \frac{10}{pulse\_width} \tag{2.45}$$

As time is passing through *dt3*, automatic time step control is activated to accelerate the simulations. The same method is used in the evaluation of the automatic time step, *Δt*:

$$\frac{1}{\Delta t} = \frac{1}{10^{-9}} + 100 \cdot \frac{dJ(t)}{dt} \qquad (2.46)$$

where 1ns is the time step used in steady states simulations for fast convergence, and the second term describes the current change with respect to time. Figure 2.5 below shows how the automatic time step varies for current changes orders of magnitude.

Figure 2.5   Automatic time step Δt vs. current changes.

2.6. Numerical Solution Techniques

In this section, LU Decomposition method, as the solution technique of discretized differential equations such as the discretized Poisson's equation and continuity equations, will be discussed. The implementation of Gummel's scheme will also be introduced.

2.6.1 LU Decomposition Method

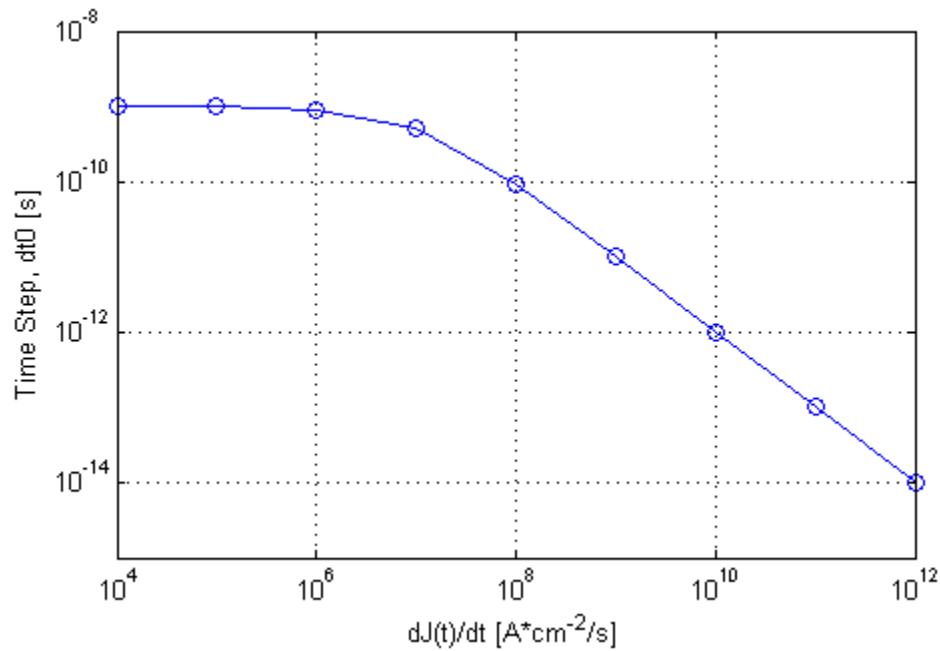As derived above in section 2.2 and 2.3, both Poisson's equation and continuity equations can be written in matrix form as,

$$[A][x]=[F] \tag{2.47}$$

where A is the coefficients matrix, x is the solution and F is the forcing function. Gauss Elimination Method[21] can be employed to solve this matrix equation. However it has the disadvantage that all right-hand sides, the forcing function in this case, must be known in advance for the elimination steps to proceed. The LU Decomposition Method[22] has the property that the matrix decomposition step can be performed independent of the forcing functions.

Square matrix equations as in Equation 2.12 and 2.48, can be solved by breaking the tridiagonal square coefficient matrix $[A]$ into lower triangular and upper triangular matrices, usually named as $[L]$ and $[U]$ matrices,

$$[A]=[L][U] \tag{2.48}$$

And the original Equation 2.48 becomes,

$$[L][U][x]=[F] \tag{2.49}$$

Equation 2.50 can be further broken into two problems,

$$
\begin{aligned}
[L][y]&=[F]\\
[U][x]&=[y]
\end{aligned} \tag{2.50}
$$

$[y]$ can be solved with a simple forward substitution step at first and then $[x]$ can be evaluated by a backward substitution algorithm easily. Recall the discretized Matrix form of Poisson's equation,

$$
\begin{pmatrix}
b_1 & c_1 & & & & & & 0 \\
a_2 & b_2 & c_2 & & & & & \\
& a_3 & b_3 & c_3 & & & & \\
& & \ddots & \ddots & & & & \\
& & & a_{n-2} & b_{n-2} & c_{n-1} & & \\
& & & & a_{n-1} & b_{n-1} & c_{n-1} & \\
0 & & & & & a_n & b_n
\end{pmatrix}
\begin{pmatrix}
\phi_1^{new} \\
\phi_2^{new} \\
\vdots \\
\vdots \\
\vdots \\
\phi_{n-1}^{new} \\
\phi_n^{new}
\end{pmatrix}
=
\begin{pmatrix}
f_1 \\
f_2 \\
\vdots \\
\vdots \\
\vdots \\
f_{n-1} \\
f_n
\end{pmatrix}
\tag{2.51}
$$

Decompose the coefficient matrix into a product of lower and upper triangular matrices:

$$
[A] = [L][U] =
\begin{bmatrix}
1 & 0 & 0 & 0 & \cdots & 0 \\
\beta_2 & 1 & 0 & 0 & \cdots & 0 \\
0 & \beta_3 & 1 & 0 & \cdots & 0 \\
\vdots & & & & & \\
\vdots & & & & & \\
0 & 0 & 0 & \cdots & \beta_n & 1
\end{bmatrix}
\begin{bmatrix}
\alpha_1 & c_1 & 0 & 0 & \cdots & 0 \\
0 & \alpha_2 & c_2 & 0 & \cdots & 0 \\
0 & 0 & \alpha_3 & c_3 & \cdots & 0 \\
\vdots & & & & & \\
\vdots & & & & & \\
0 & 0 & 0 & \cdots & 0 & \alpha_n
\end{bmatrix}
\tag{2.52}
$$

where,

$$
\begin{aligned}
\alpha_1 &= b_1 \\
\beta_k &= a_k / \alpha_{k-1} \\
\alpha_k &= b_k - \beta_k c_{k-1} \\
k &= 2, 3, ..., n
\end{aligned}
\tag{2.53}
$$

Now we can have the $[L][y]=[F]$ as following,

$$
\overset{\overset{L}{\Downarrow}}{
\begin{pmatrix}
1 & & & & \\
\beta_2 & 1 & & 0 & \\
& \cdots & \cdots & & \\
& 0 & \beta_{n-1} & 1 & \\
& & & \beta_n & 1
\end{pmatrix}}
\overset{\overset{y}{\Downarrow}}{
\begin{pmatrix}
y_1 \\
y_2 \\
\cdots \\
\cdots \\
y_n
\end{pmatrix}}
=
\overset{\overset{F}{\Downarrow}}{
\begin{pmatrix}
f_1 \\
f_2 \\
\cdots \\
\cdots \\
f_n
\end{pmatrix}}
\tag{2.54}
$$

Using forward substitution, solutions can be easily obtained:

$$y_1 = f_1$$
$$y_i = f_i - \beta_i y_{i-1}$$
$$i = 2, 3, \ldots, n$$

(2.55)

Then we have the matrix of $[U][\phi]=[y]$ as,

$$
\overset{U}{\Downarrow}
\begin{pmatrix}
\alpha_1 & c_1 & & & \\
& \alpha_2 & c_2 & 0 & \\
& & \cdots & \cdots & \\
& 0 & & \alpha_{n-1} & c_{n-1} \\
& & & & \alpha_n
\end{pmatrix}
\overset{\phi}{\Downarrow}
\begin{pmatrix}
\phi_1 \\
\cdots \\
\cdots \\
\phi_{n-1} \\
\phi_n
\end{pmatrix}
=
\overset{y}{\Downarrow}
\begin{pmatrix}
y_1 \\
y_2 \\
\cdots \\
\cdots \\
y_n
\end{pmatrix}
$$

(2.56)

Similarly to the solution of the lower triangular matrix, $[U]$ can be solved by backward substitution,

$$\phi_n = \frac{y_n}{\alpha_n}$$
$$\phi_i = \frac{y_i - c_i \phi_{i+1}}{\alpha_i}$$

(2.57)

Thus we have the solution for $[\phi]$ at each grid node using this method. The carrier density of electrons and holes that appear in the forcing function $[f]$ shall be updated immediately. Accurate solution is achieved within several iterations.

2.6.2   Gummel's Iteration Method

Gummel's method solves the coupled set of carrier continuity equations together with the Poisson's equation via a decoupled procedure. The potential profile obtained from equilibrium simulations is substituted into the continuity equations (Equation 2.41 and 2.42), for carriers distribution profile calculation. The result is then sent back into

Poisson's equation (Equation 2.11) to update the forcing function and the central coefficients for new electrostatic energy profiles. This process is repeated until convergence requirement is achieved, as shown in Figure. 2.6.
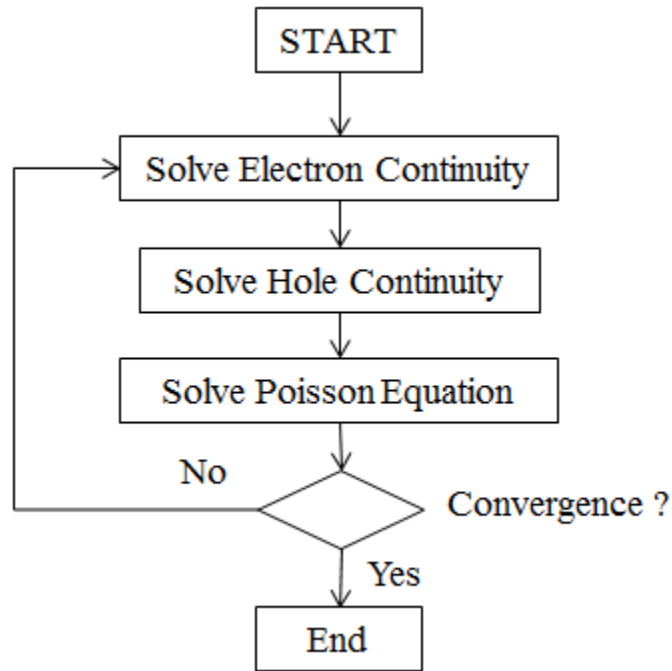

Figure 2.6   Gummel's iteration scheme.

Chapter 3   PHYSICAL MODELS

In this chapter, different kinds of physical models that we implemented in this

simulator, such as generation/recombination mechanisms, Schottky contact and partially ionized dopants will be discussed.

3.1. Generation and Recombination Mechanisms

Generation/recombination events take place when the device is under the influence of bias or illumination. They determine the performance and characteristics of devices. The simplest classification of generation and recombination mechanisms starts from the number of particles involved in the process, as shown in Figure 3.1.
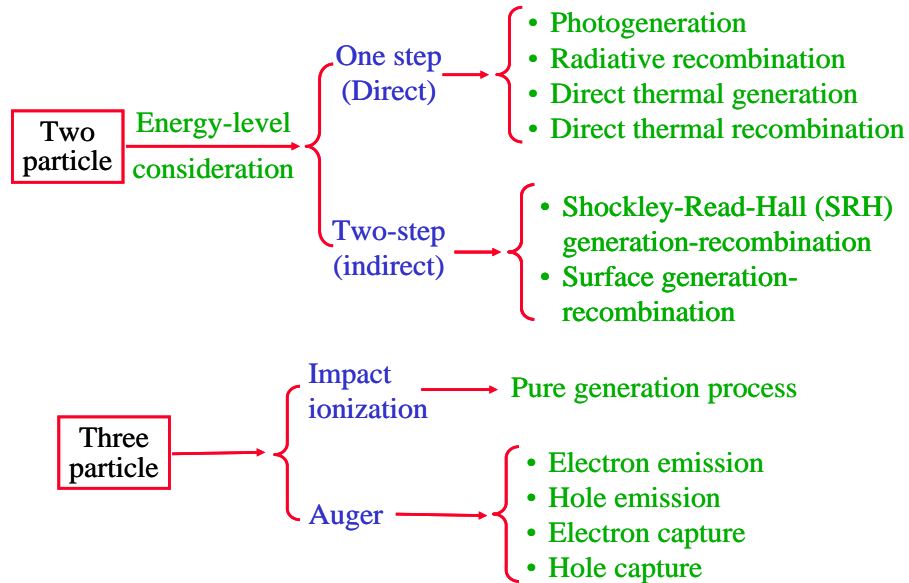

Figure 3.1   Classification of the generation/recombination process.

In this section the numerical expression for U_i, the net recombination rate in the continuity equations, will be evaluated. Shockley – Read - Hall recombination, as well as trap-assited recombination, radiative (band-to-band) recombination, surface recombination and optical generation will be introduced. Auger recombination has not been implemented since it does not dominate the bulk recombination mechanisms in

33

CdTe material.

3.1.1. Shockley – Read – Hall Recombination

The Shockley – Read – Hall (SRH) model was first introduced in 1952 by Shockley, Read[23] and Hall[24] to describe the statistics of recombination and generation of carriers in semiconductors occurring through traps, which exist in every semiconductors. These trap levels, known as recombination-generation centers, lay within the forbidden band. Trap levels are caused by crystal lattice imperfection such as doped impurities and vacancies; they facilitate the recombination of carriers, since the jump can be split into two parts, requiring lower energy, as illustrated below.
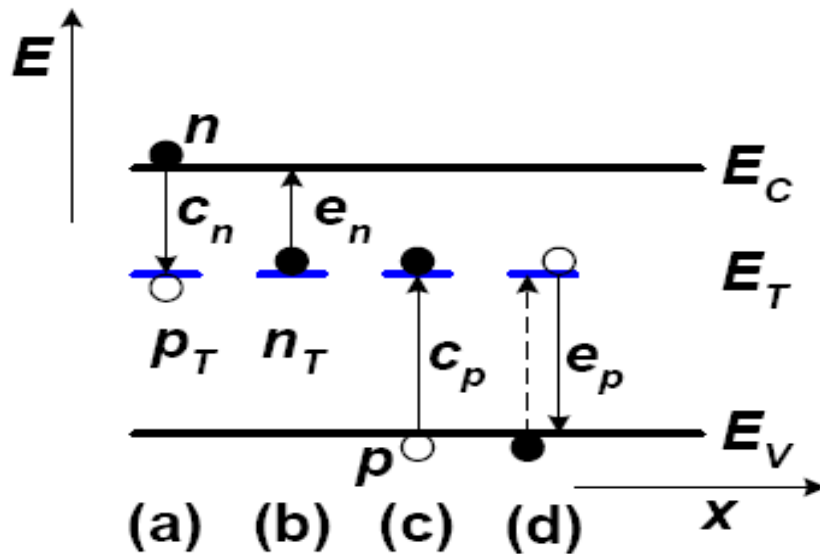

Figure 3.2   Graphical descriptions of the SRH recombination.

(Courtesy of Dr. Schroder)

These mechanisms consist of: (a) electron capture (a free electron moves from the

34

conduction band to an unoccupied trap level), (b) electron emission (a trapped electron jumps to the conduction band), (c) hole capture (a hole recombines with an electron trapped in the bandgap and (d) hole emission (a trapped hole jumps to the valence band). Physical models for these processes involve equations for electron density in the conduction band, holes in the valence band, their capture probabilities, trapped carrier density, and relative emission rates. The conventional SRH net recombination rate is given by:

$$R_{SRH} = \frac{pn - n_i^2}{\tau_p(n + n_i \exp(\frac{E_t - E_i}{kT})) + \tau_n(p + n_i \exp(\frac{-E_t + E_i}{kT}))} \qquad (3.1)$$

where, E_t is the energy level of traps, E_i is the intrinsic Fermi level, τ_n and τ_p are the minority carrier lifetimes which are heavily dependent on the density of trap centers, σ is the capture cross section for different type of carriers and V_{th}, is the thermal velocity,

$$\begin{aligned} \tau_n &= \frac{1}{\sigma_n V_{th} N_T} \\ \tau_p &= \frac{1}{\sigma_p V_{th} N_T} \end{aligned} \qquad (3.2)$$

A simple model could be employed without the consideration of trap energy levels and the occupations of trap states when $E_t = E_i$:

$$R_{SRH} = \frac{pn - n_i^2}{\tau_p(n + n_i) + \tau_n(p + n_i)} \qquad (3.3)$$

3.1.2. Optical Generation

35

Carriers can be generated in semiconductors by illumination with light; this process is called photo-generation. An incoming photon with sufficient energy can excite electrons from valence band into the conduction band. Optical absorption can be a direct or indirect process, depending on the band structure of the semiconductor. With indirect bangdap materials, as Silicon, additional phonons are required to conserve the momentum in the process of carrier generation, as shown in the right panel of Figure 3.3, while phonons do not play big roles in the absorption of direct bandgap materials, such as GaAs, Germanium and CdTe, as illustrated in the left panel of Figure 3.3. For this reason, the band edge absorption coefficient for direct bandgap semiconductors is significantly larger than that of indirect gap materials.
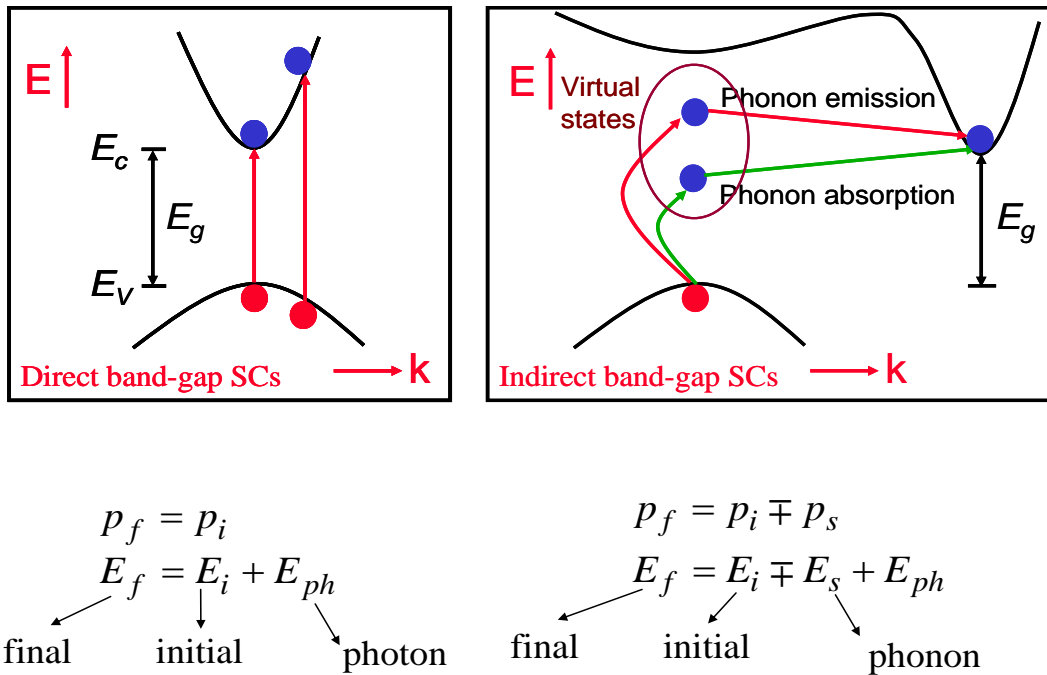

$$p_f = p_i$$
$$E_f = E_i + E_{ph}$$

final   initial   photon

$$p_f = p_i \mp p_s$$
$$E_f = E_i \mp E_s + E_{ph}$$

final   initial   phonon

Figure 3.3   Photon absorptions in direct bangdap and indirect gap semiconductors.

Usually, the sufficient energy to excite electrons must be the bandgap energy, E_g. Due to the existence of Urbach tail[25], photons with energy less than bandgap can be

absorbed, as the large absorption coefficients below bandgap depicted in Figure 3.4. The generation was determined by the absorption coefficients of the materials[26]:

$$G(E, x) = \frac{(1 - R(E))\alpha(E)}{EA} P_{opt}(E) \exp(-\alpha(E)x) \tag{3.4}$$

where E is the incoming photon energy, $\alpha(E)$ is the absorption coefficient of the material at the incoming photon energy, $R(E)$ is the reflection rate of certain photon energy at the front surface, A is the area of the illumination, $P_{opt}(E)$ is the light intensity for photons at the front surface. By numerical integrals over photon energy, we can determine the total generation rate, $G(x)$.
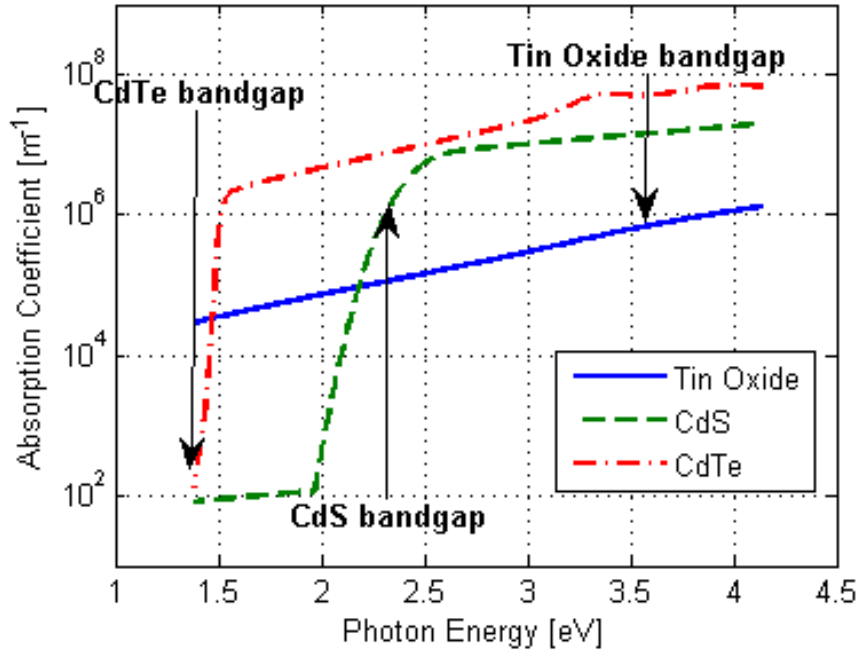
Figure 3.4   Absorption coefficients SnO, CdS and CdTe.

3.1.3. Band-to-Band Recombination

Contrary to optical generation, Band-to-band recombination annihilates electron-hole pairs, with photons generated at the bandgap energy[27] – this is how LEDs and semiconductor lasers operate. It is also the major mechanism for Photoluminescence decay. Since both electrons and holes are required in this process, the recombination rate is proportional to the excess carrier density, and can be expressed as,

$$U_{bb} = b_{rad}(np - n_i^2) \qquad (3.5)$$

where b_{rad} is the bimolecular recombination constant. Since these generated photons have energy near the bandgap, it is possible to reabsorb these photons before they exit the solar cell. A well designed direct bandgap photovoltaic solar cell can take advantage of this photon recycling and increase the carrier lifetimes[28].

With the derivation of radiative recombination, the net generation rates term in continuity equations, can be finally expressed as,

$$U_i = R_i^{SRH} + U_i^{bb} - G_i^{opt} \qquad (3.6)$$

3.1.4. Surface Recombination

In real devices, defects are much more likely to stay at the interface between different crystal lattices, for example, we might have broken bonds at semiconductor-metal contacts. In such cases, the trap states are constrained onto a 2D surface rather than 3D bulk. It is also much more meaningful to express these r – g centers in terms of density per unit area than per unit volume. Unlike SRH recombination and optical generation, the relevant quantity that determines recombination velocity should be flux, instead of a volume recombination rate.

Assume a surface contains Ns traps per unit area, then within an infinite thin layer δx around the surface, the recombination flux should be

$$U_s \delta x = \frac{n_s p_s - n_i^2}{\frac{1}{S_n}(p_s + p_t) + \frac{1}{S_p}(n_s + n_t)} \tag{3.7}$$

per unit area, where n_s, n_p are the carrier densities at the surface, S_n, S_p are the surface recombination velocity in unit of meter per second, defined as,

$$S_n = B_n N_s$$
$$S_p = B_p N_s \tag{3.8}$$

In p-type CdTe material, Equation 3.6 can be reduced to

$$U_s \delta x = S_n(n_n - n_0) \tag{3.9}$$

where n_0 is the minority carrier concentration, electron density in this case, under equilibrium. This leakage of minority carriers to the surface results in surface recombination current, derived as,

$$J_n(x_s) = -q S_n(n_n - n_0) \tag{3.10}$$

Substitute Equation 3.9 into the electrons continuity equation,

$$J_{i-1/2}^n = \frac{q D_{i-1/2}^n}{dx_{i-1}}\left(n_i B\left(\frac{\phi_i^n - \phi_{i-1}^n}{V_T}\right) - n_{i-1}B\left(\frac{\phi_{i-1}^n - \phi_i^n}{V_T}\right)\right) \tag{3.11}$$

to arrive at

$$-S_n(n_i - n_0) = \frac{D_{i-1/2}^n}{dx_{i-1}}\left(n_i B\left(\frac{\phi_i^n - \phi_{i-1}^n}{V_T}\right) - n_{i-1}B\left(\frac{\phi_{i-1}^n - \phi_i^n}{V_T}\right)\right) \tag{3.12}$$

Which can be written as,

$$D_{i-1/2}^n B\left(\frac{\phi_{i-1}^n - \phi_i^n}{V_T}\right) n_{i-1} - [D_{i-1/2}^n B\left(\frac{\phi_i^n - \phi_{i-1}^n}{V_T}\right) + S_n dx_{i-1}] n_i = S_n dx_{i-1} n_0 \qquad (3.13)$$

The coefficients in Equation 3.13 should be the boundary conditions of the discretized electron continuity equation, of the form

$$
\begin{aligned}
an_i &= D_{i-1/2}^n B\left(\frac{\phi_{i-1}^n - \phi_i^n}{V_T}\right) \\
bn_i &= -[D_{i-1/2}^n B\left(\frac{\phi_i^n - \phi_{i-1}^n}{V_T}\right) + S_n dx_{i-1}] \qquad (3.14)\\
cn_i &= 0 \\
fn_i &= S_n dx_{i-1} n_0
\end{aligned}
$$

where i denotes the surface node in the meshing. Similar derivation can be made for the hole continuity equation.

It is important to mention that this mechanism must be combined with a Schottky contact, since a particular value of surface recombination velocity results in excess minority carriers at the contact; this contradicts with the Ohmic contact model that assumes no excess minority carriers exists at the boundary.

3.2. Ohmic and Schotky Contact

Many of useful properties of p-n junctions can be achieved by forming different metal-semiconductor contacts[29]. The major difference between ohmic and Schottky contact is the Schottky barrier height, ϕ_B, is non-positive or positive. For Ohmic contacts, the barrier height should be near zero or negative, forming accumulation type contacts, thus the majority carriers are free to flow out the semiconductors, as shown below in

Figure 3.5. While for Schottky contacts, on the contrary, the barrier height would be positive, forming depletion type contacts, so that the majority carriers cannot be absorbed freely due to the band bending caused by positive barrier height. Hence, the way we implemented them in our simulator is different.
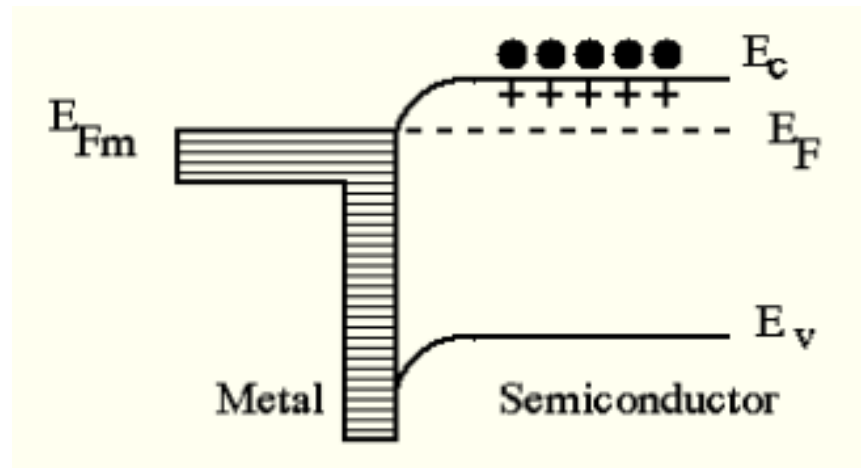

Figure 3.5   Accumulation type Ohmic contact.

3.2.1. Modeling of Ohmic Contact

Although the barrier height could be negative for an Ohmic contact, we can treat them simply as flat band, with the carrier concentration and electrostatic potential under equilibrium.

For the discretized Poisson's Equation, we applied the Dirichlet Boundary Conditions[30], that the coefficient matrix elements at boundary are fixed as the equilibrium results, during the iterative calculations, as the following Equation 3.15, where "*1*" denotes the first grid nodes and *nmax* represents the last grid point.

$$a_1 = 0 \quad a_{n\max} = 0$$
$$b_1 = 1 \quad b_{n\max} = 1$$
$$c_1 = 0 \quad c_{n\max} = 0 \tag{3.15}$$
$$f_1 = \phi_1 \quad f_{n\max} = \phi_{n\max}$$

The carrier concentrations at the contact have been fixed at the equilibrium value for the discretized continuity equation, preventing any excess minority carriers' existence. The following is an example of boundary conditions for the electron continuity equation of a p-n diode,

$$an_1 = 0 \quad an_{n\max} = 0$$
$$bn_1 = 1 \quad bn_{n\max} = 1$$
$$cn_1 = 0 \quad cn_{n\max} = 0 \tag{3.16}$$
$$fn_1 = n_{p0} \quad fn_{n\max} = n_{n0}$$

where n_{p0} is the equilibrium electron concentration (minority carrier dentisy) at p-type material and n_{n0} is the equilibrium majority concentration in the n side. Similar boundary conditions can be defined for holes.

$$ap_1 = 0 \quad ap_{n\max} = 0$$
$$bp_1 = 1 \quad bp_{n\max} = 1$$
$$cp_1 = 0 \quad cp_{n\max} = 0 \tag{3.17}$$
$$fp_1 = P_{p0} \quad fp_{n\max} = P_{n0}$$

3.2.2. Modeling of Schottky Contact

Due to the self-compensation mechanism[31], CdTe is usually lightly doped in solar cells. Thus a Schottky must be formed due to the difference in working functions of metal contact and CdTe. A Schottky contact, similar to an Ohmic contact, is a Dirichlet

boundary contition in the discretized Poisson's equation. The electrostatic potential is fixed at a certain value hence the derivation of the forcing function is crucial for the Schottky contact model. Let's begin with the barrier height,

$$\phi_B = E_F - E_V \tag{3.18}$$

It can be written as,
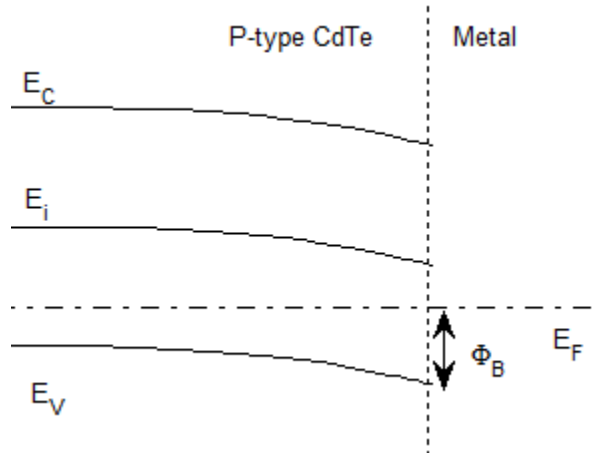
$$\phi_B = (E_F - E_i) + (E_i - E_V) \tag{3.19}$$

Figure 3.6   P-doped depletion type Schottky contact.

knowing that $\phi = E_F - E_i$ and $E_i - E_V = E_g/2$, Equation 3.18 arrives,

$$\phi_{n\max} = \phi_B - \frac{E_g}{2} \tag{3.20}$$

Thus the forcing function at the Schottky contact for Poisson's equation will be,

$$f_{n\max} = \phi_B - \frac{E_g}{2} \tag{3.21}$$

All the other elements in the matrix form of Poisson's equation should retain the same as Ohmic contact case. While for non-equilibrium, surface recombination can be applied

together with Schottky contact.

3.3. Partial Ionization of Dopants

As one kind of impurities, dopants are governed by distribution function of impurities, which differs from the Fermi - Dirac distribution. Due to the electron spin state, a modified distribution function for dopants can be given by,

$$f_{donor}(E_D) = \frac{1}{1 + g_D \exp(\dfrac{E_F - E_D}{V_T})}$$

$$f_{acceptor}(E_A) = \frac{1}{1 + g_A \exp(\dfrac{E_A - E_F}{V_T})}$$

(3.22)

Hence we can have the activated dopants density,

$$N_D^+ = \frac{N_D}{1 + g_D \exp(\dfrac{E_F - E_D}{V_T})}$$

$$N_A^- = \frac{N_A}{1 + g_A \exp(\dfrac{E_A - E_F}{V_T})}$$

(3.23)

where g_D and g_A are the degeneracy factor for donors and acceptors, E_D and E_A are the actual dopants energy level.

The partial ionization of dopants works with Fermi – Dirac statistics in the charge neutrality equations for the solution of electrostatic potentials, which will be the initial guess in the Poisson equation solver. For a piece of n-type semiconductor, the charge neutrality equation is,

$$\rho = -n + N_D^+ = 0$$

(3.24)

44

taking the Fermi – Dirac distribution of electrons and partial ionization donors into consideration, we get,

$$\frac{N_D}{1 + g_D \exp(\frac{E_F - E_D}{V_T})} - N_C F_{1/2}(\frac{E_F - E_C}{V_T}) = 0 \tag{3.25}$$

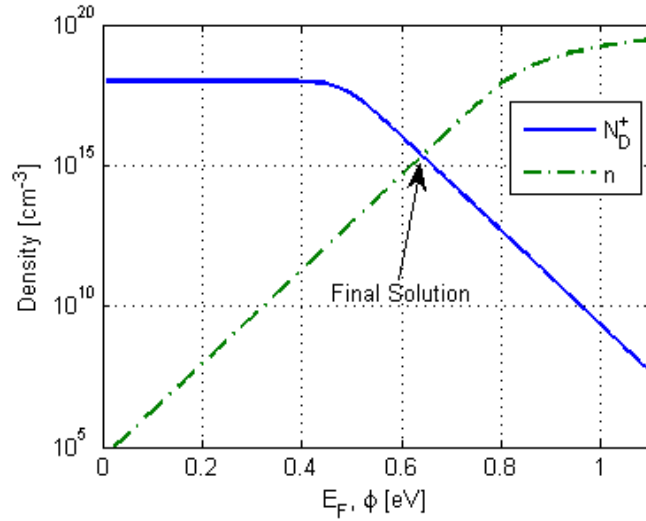Equation 3.25 can be solved iteratively or graphically, as shown below.

Figure 3.7   Solution of ϕ with partial ionized dopants and Fermi-Dirac statistics.

A similar evaluation of holes and acceptors can be made. It is necessary to update the dopant profile, C_i in Poisson's equation, with any new electrostatic potential profiles obtained, both in the equilibrium solver and in non-equilibrium simulators. In this project, copper was employed as the acceptors in P-type CdTe[32]. And its activation energy level was set to be 0.1 eV above the valence band.

45

Chapter 4   SIMULATION RESULTS

It is important for simulators to have accurate material parameters to generate appropriate results. Much research has been conducted for cadmium telluride solar cell materials' electronic properties recently. Thus we combined a variety of sources[33-35], and came up with a set of reasonable numbers for common CdTe solar cells. Table 4.1 below shows the standard device configuration and the material parameters for equilibrium simulations.

Table 4.1   Device parameters for equilibrium simulations.

Temperature = 300 K	SnO2	CdS	CdTe
Layer thickness (μm)	0.1	0.2	3.6
Bandgap (eV)	3.6	2.38	1.46
Electron Affinity (eV)	4.5	4.5	4.28
Doping Density (cm^{-3})	N-type: 10^{17}	N-type: 10^{17}	P-type: 3×10^{14}
Relative Permittivity	9.6	9.0	10.3
Conduction Band DOS (cm^{-3})	2.24×10^{18}	2.62×10^{18}	1.07×10^{18}
Valence Band DOS (cm^{-3})	2.51×10^{19}	1.72×10^{19}	6.08×10^{18}
Dopants Acitivation Energy (eV)	0.03	0.03	0.1
Schottky Barrier Height (eV)	-	-	0.44

For non-equilibrium simulations, typical material properties for CdTe solar cells are shown in Table 4.2. In this project, all parameters used are given in these two tables, unless mentioned otherwise.

Table 4.2   Materials properties for non-equilibrium simulations.

Temperature = 300 K	SnO2	CdS	CdTe
Electron Mobility (cm^2/Vs)	100	100	100
Hole Mobility (cm^2/Vs)	60	60	50
Electron Lifetime (s)	10^{-9}	10^{-9}	10^{-9}
Hole Lifetime (s)	10^{-8}	10^{-8}	5×10^{-9}
Radiative Recombination Rate (cm^3/s)	4.72×10^{-11}	4.72×10^{-11}	4.72×10^{-11}
Surface Recombination Velocity (cm/s)	-	-	10^7

4.1. Equilibrium Simulation Results
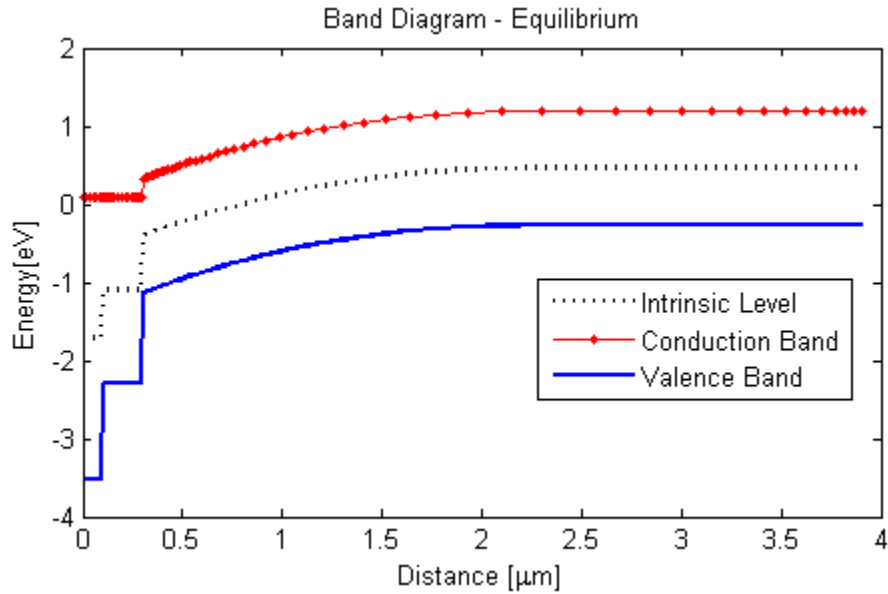
Figure 4.1   Equilibrium energy band diagram.

By solving the Poisson equation solely, equilibrium results can be achieved. Shown in Figures 4.1-4.3 are the energy band diagram, the electric field profile and the carrier densities. The back contact was assumed to be Ohmic, so that flat band is

observed. All energy levels above are referenced with respect to the Fermi level, which equals to zero along the entire device.
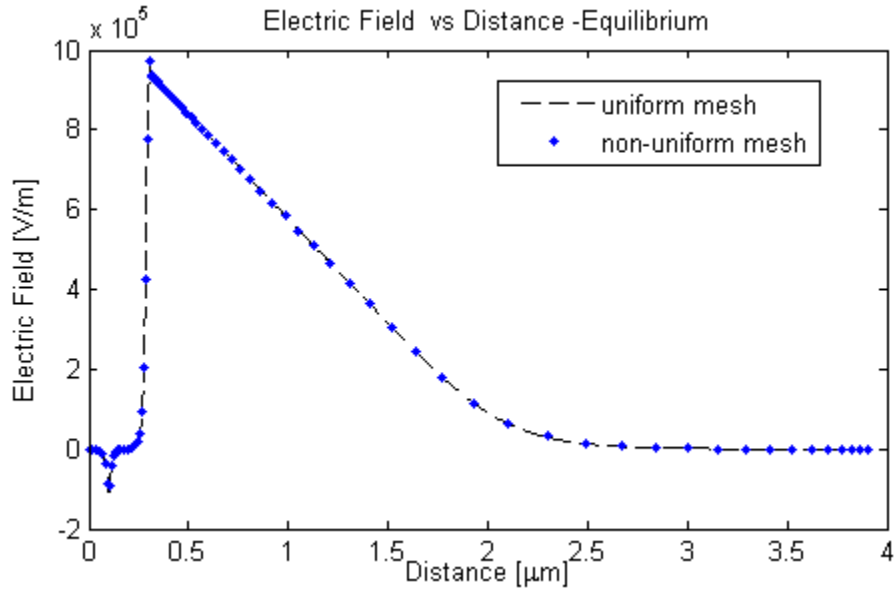
Figure 4.2   Electric field profile for uniform and non-uniform mesh at equilibrium.
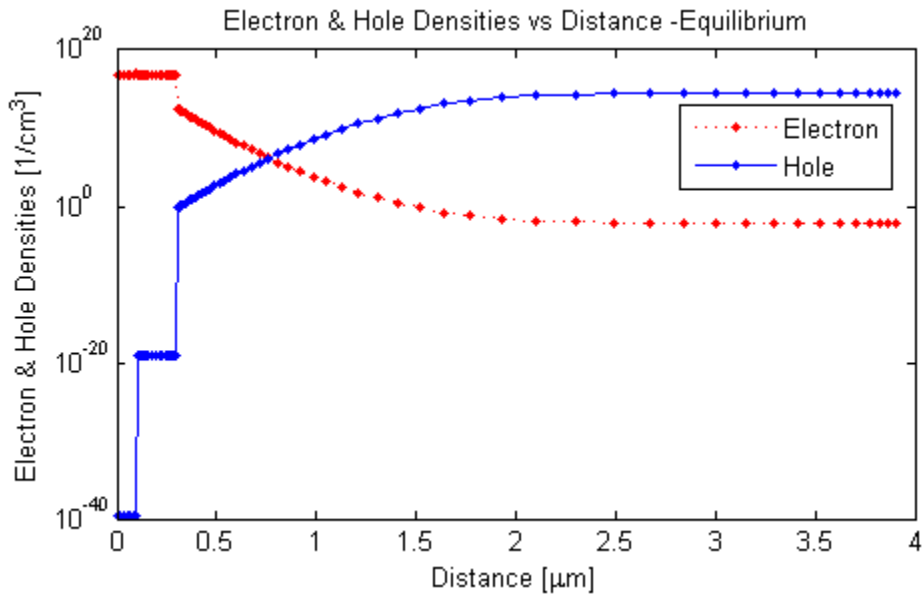
Figure 4.3   Carrier distributions at Equilibrium.

The number of grid points has been reduced from 688 to 74 with the non-uniform

strategy we developed. We also modeled the equilibrium with Schottky contact and the results of these simulations are as shown in Figure 4.4-4.6. The number of grid points increased to 79 due to the increasing electric field near Schottky contact. Both band bending and depleted majority carrier concentration were observed.
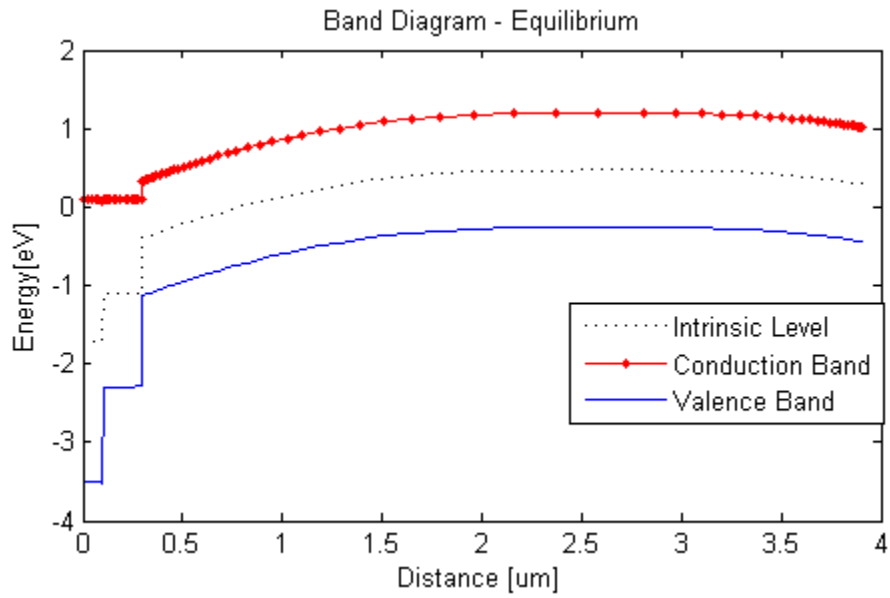
Figure 4.4   Equilibrium band diagram with Schottky contact applied.
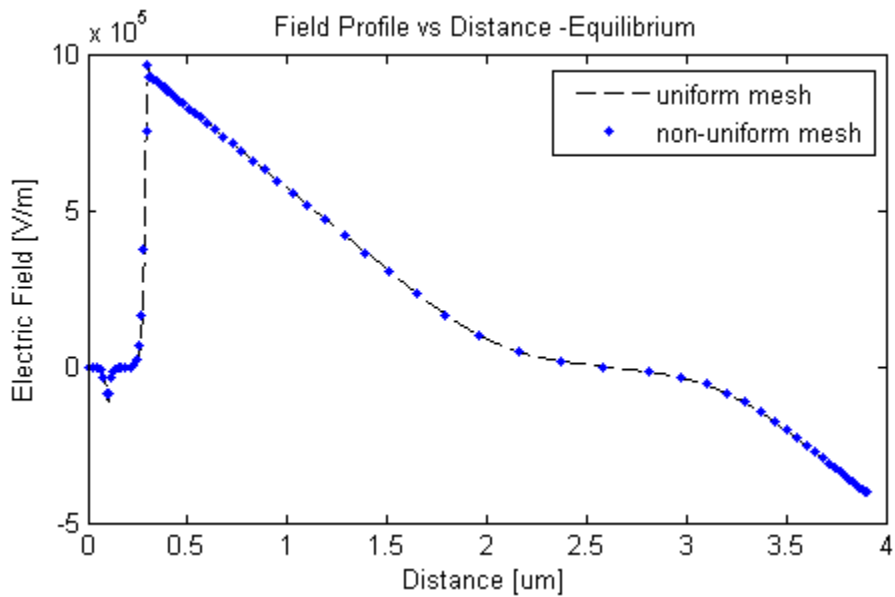
Figure 4.5   Electric field profiles at equilibrium with Schottky contact applied.

49
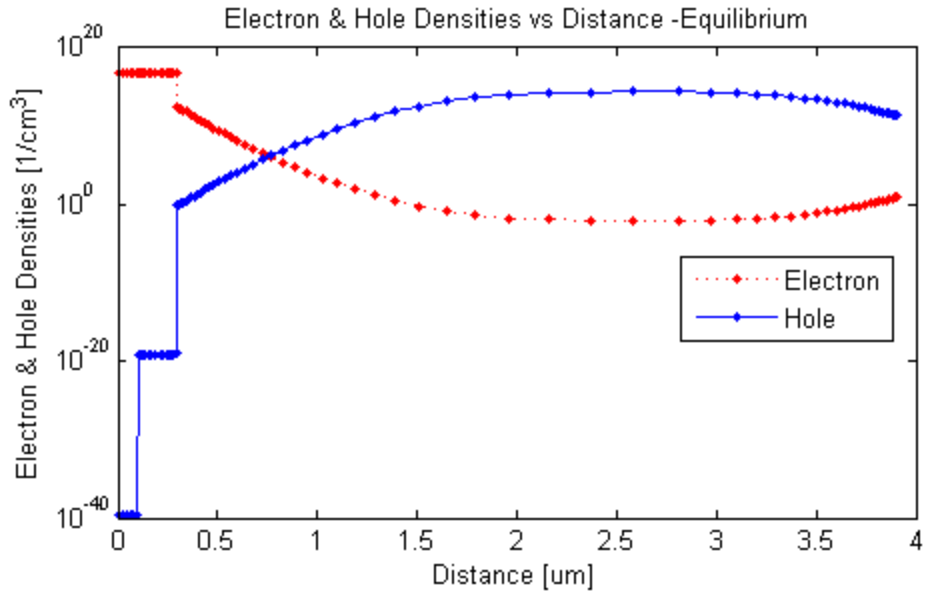
Figure 4.6   Carrier distributions at equilibrium with Schottky contact applied.

We could also achieve the accumulation type Ohmic contact by adjusting the barrier height to near zero value, as depicted in Figure 4.7 below.
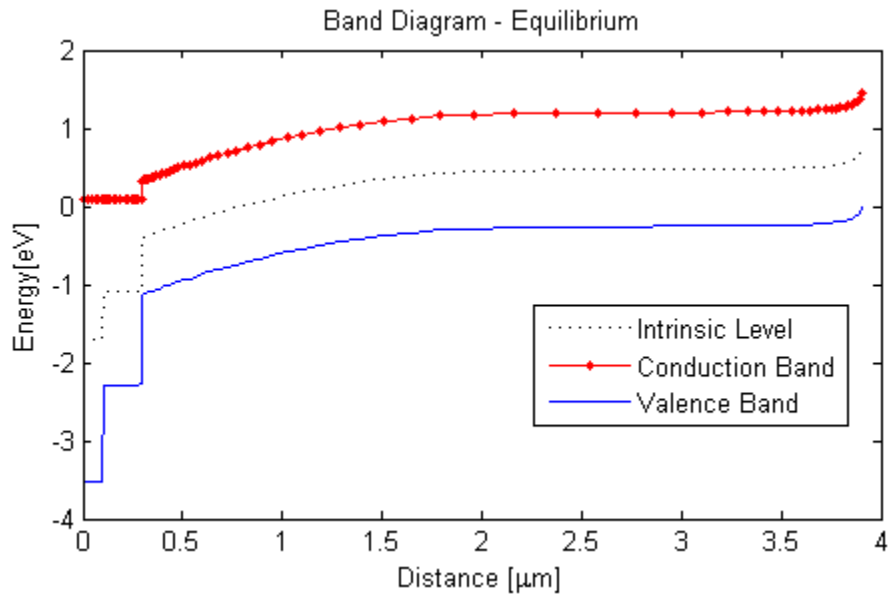
Figure 4.7   Equilibrium band diagram with accumulation type Ohmic contact

4.2.   Steady-State Simulation Results

In this section, the current – voltage characteristics of the standard cadmium telluride solar cell will be simulated both under dark and under AM1.5G solar spectrum. The results will also be compared with Atlas.

4.2.1   Under dark
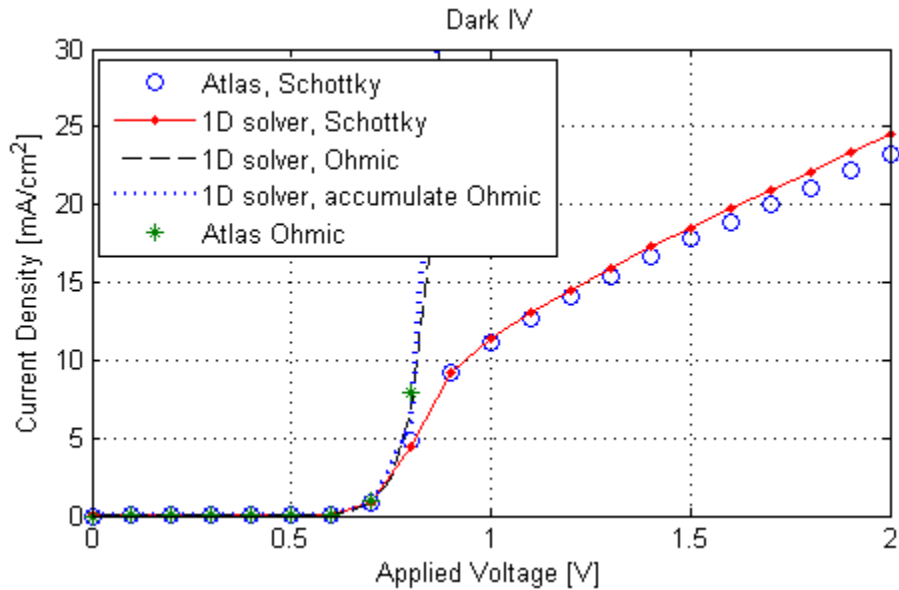
Figure 4.8   Comparisons between dark IV-characteristics.

As shown in Figure 4.8, the flat band Ohmic contact model was equivalent to the accumulative type Ohmic contact, while the Schottky contact reduced the current density at strong biases significantly[36, 37]. The Schottky barrier also helped the solver at small bias by avoiding negative currents near zero. As illustrated in Figure 4.9 below, both Ohmic contact models experienced unstable current below 0.3 V forward bias, which probably is caused by their more conducting nature. Also, the exponential relationship between bias and current is well observed for Schottky contact below threshold and for

Ohmic contact above 0.3 V. Figure 4.10 depicted the achievement of current conservation along the entire device.
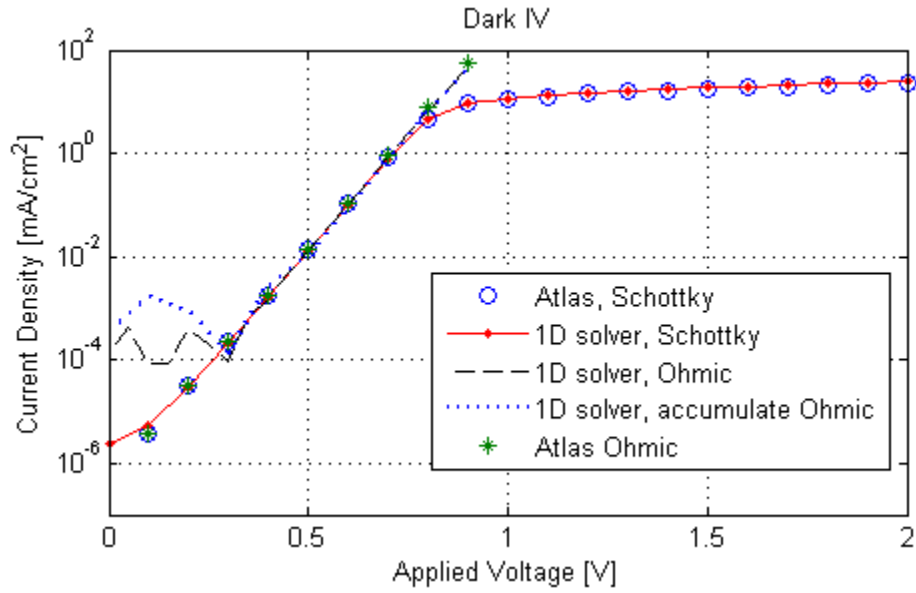

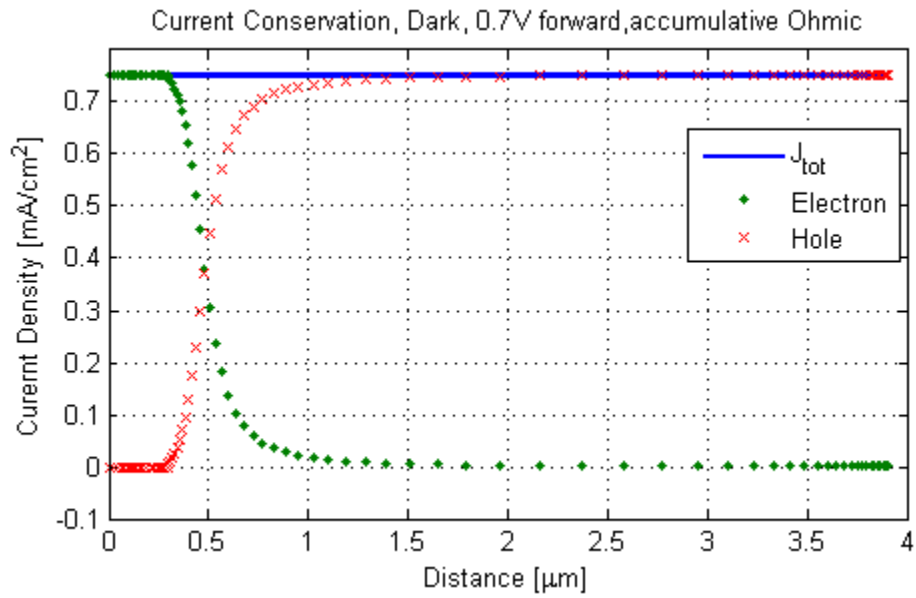Figure 4.9　　Semi log plot of dark IV-characteristics.

Figure 4.10　　Current conservation along the entire device.

4.2.2   Under illumination

For the SnO/CdS/CdTe standard configuration with thickness of 0.1/0.2/3.6 micron and doping concentrations of $10^{17}/10^{17}/3 \times 10^{14}$ cm^{-3}, the illuminated IV characteristics are shown below in Figure 4.11. Current degradation caused by depleted Schottky contact is well observed, which can be explained by the carrier distribution figure below. The major performance characteristics shown in Table 4.3 are consistent with those from Table 1.1.
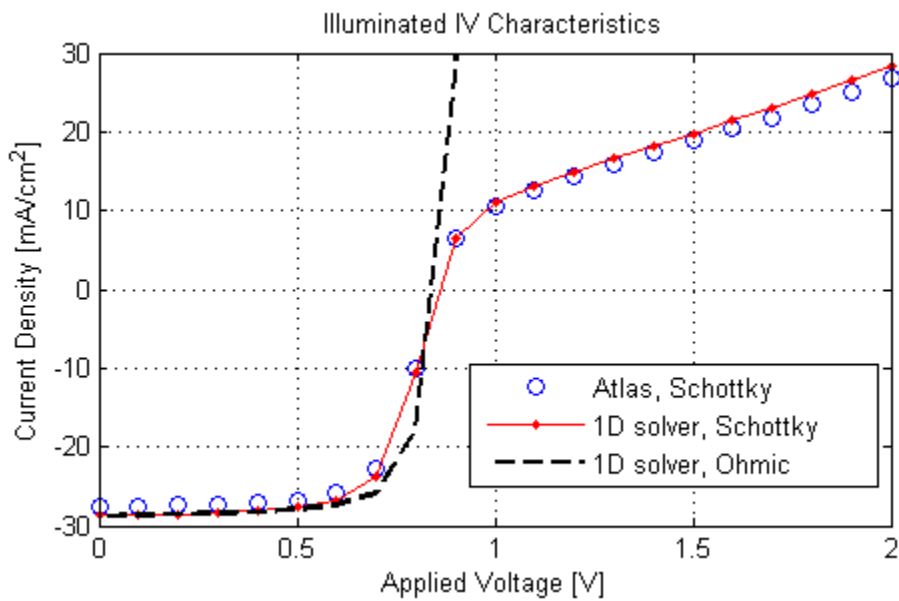

Figure 4.11   Illuminated IV characteristics of CdTe solar cell.

Table 4.3   Schottky contact's effect on key performance characteristics.

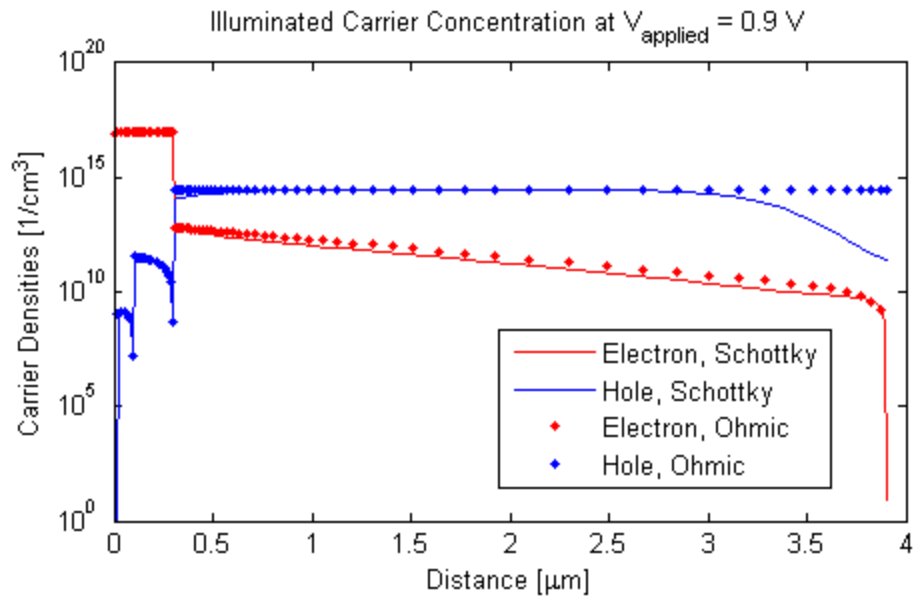|	J_{sc} (mA/cm^2)	V_{oc} (V)	Efficiency (%)	Fill Factor
Ohmic	28.77	0.8612	18.11	0.7310
Schottky	28.02	0.8596	16.62	0.6901

Figure 4.12   The difference in carrier densities at strong bias.

As illustrated above majority carrier, holes were depleted near the contact, while large amount of excess minority carriers existed due to the band bending caused by the Schottky contact. The shift in the maximum power points is depicted in Figure 4.13.
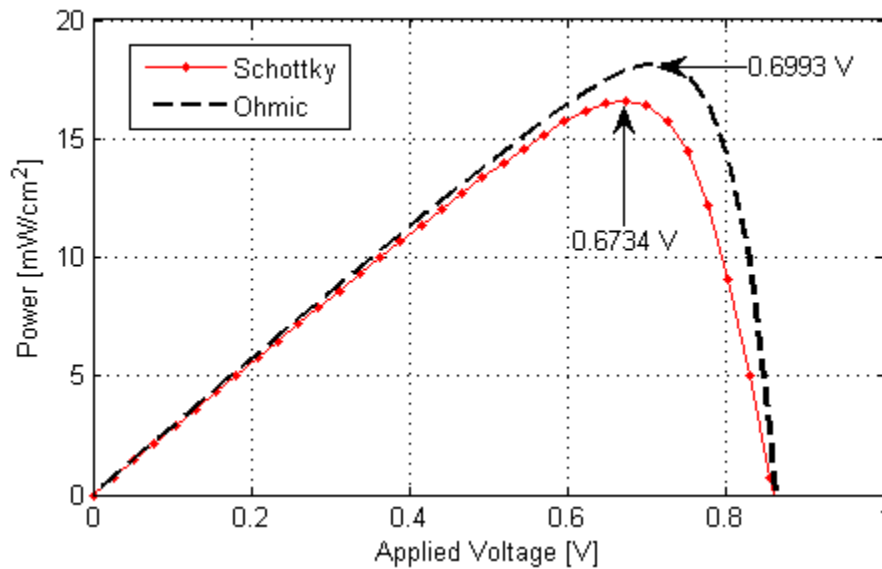

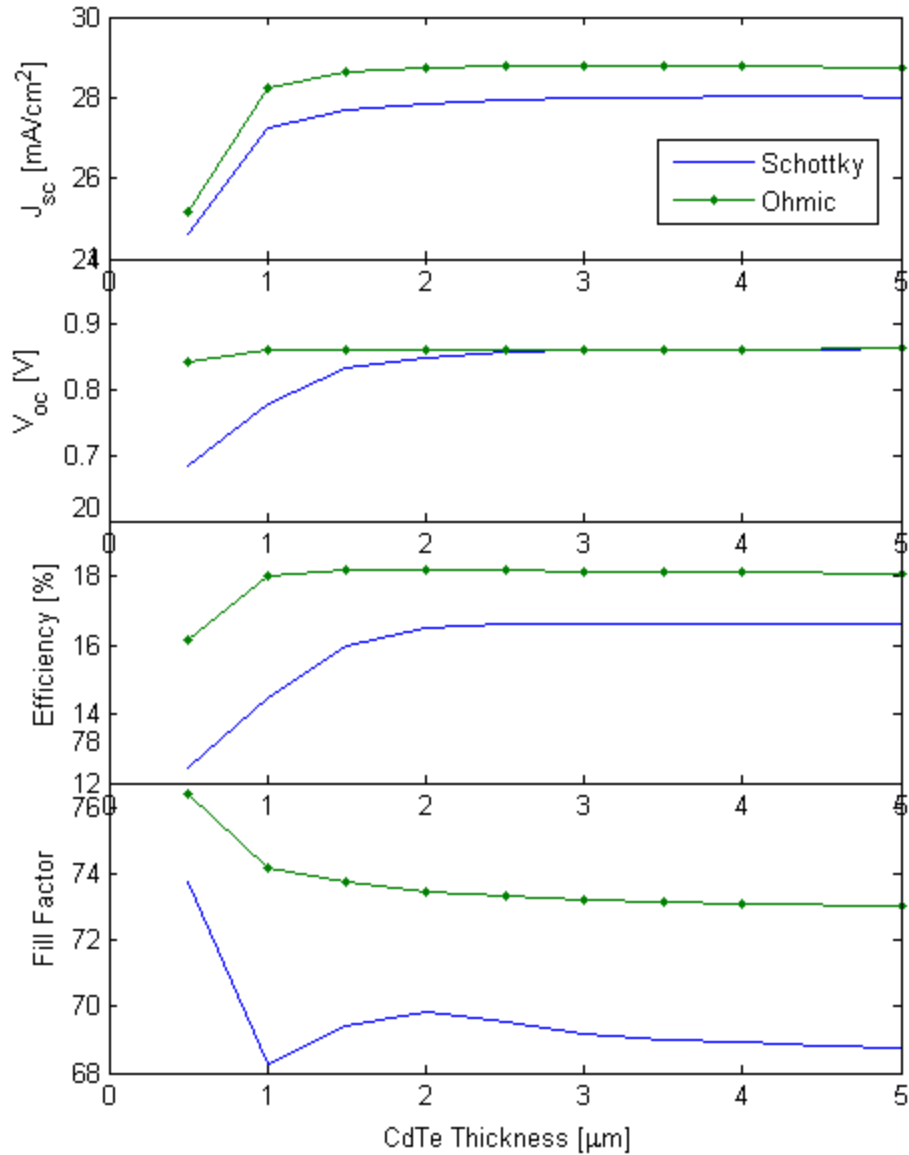Figure 4.13   Power – voltage characteristics of CdTe solar cell

Figure 4.14   The effect of CdTe thickness on the solar cells

The CdTe layer thickness was changed from 0.5 μm to 5 μm; results are shown in

Figure 4.14. All solar cell characteristics were kept almost unchanged at the thickness of

2 − 5 μm. However, due to the lack of the absorption of long wavelength photons, both

V_{oc} and J_{sc} decreased drastically below the thickness of 2 μm, which eventually leads to

the reduction in efficiency. Also, thinner CdTe layer, representing shorter length in the

direction of current flow, led to smaller internal series resistance of the solar cell, governed by the relationship between resistivity and resistance; this results in flat currents at weak bias, resulting in higher fill factor for smaller CdTe thickness.
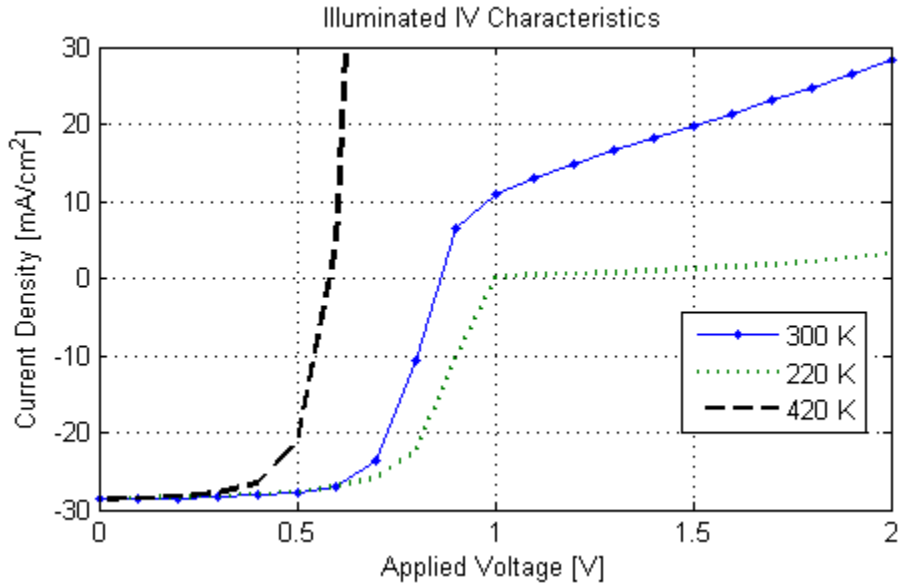

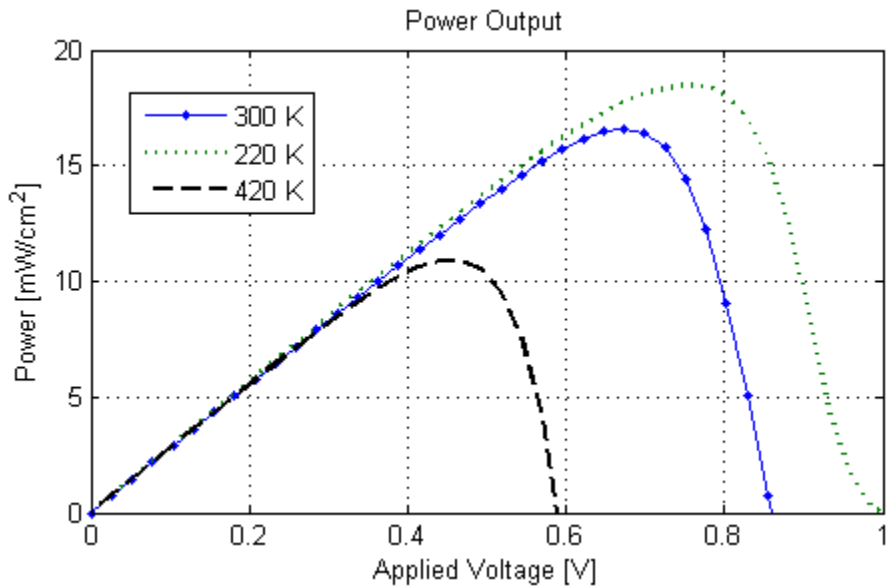Figure 4.15   IV characteristics under different temperature.

Figure 4.16   Power – voltage characteristics under different temperature.

Due to the implementation of Fermi – Dirac statistics, we were able to produce IV characteristics under different temperature. The degradation of the device performance caused by high temperature is well observed, as shown above in Figure 4.16.

4.3. Transient Simulation Results

4.3.1. Step Bias Response

The classic step function current densities of a p-n junction are reproduced by this simulator in this section. Due to small ΔV and pulse width applied, current overshoot is barely observed in Figure 4.17.
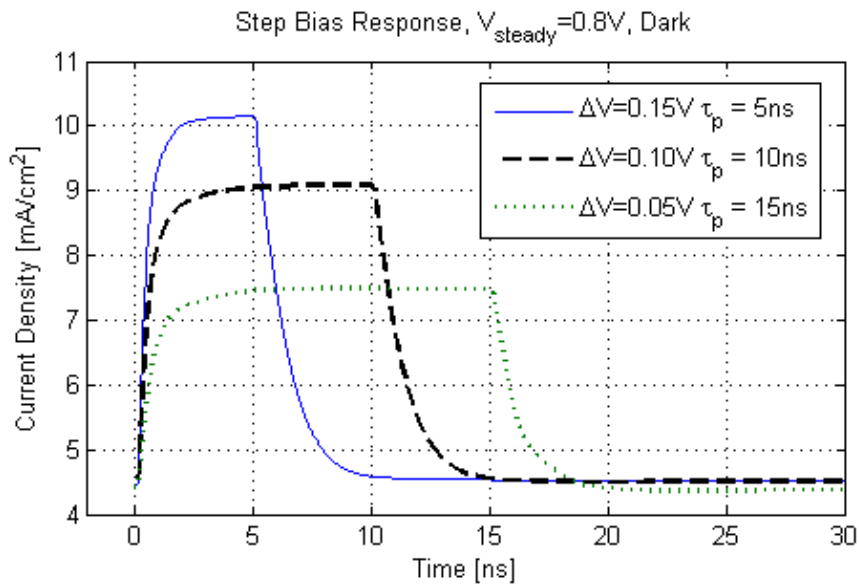

Figure 4.17   Current transients for small pulse signals.

With similar ΔV and larger pulse widths applied, the turn on characteristics of p-n diodes are well observed: it only took several nanoseconds to reach 90 percent of the current increments, as illustrated in Figure 4.18.
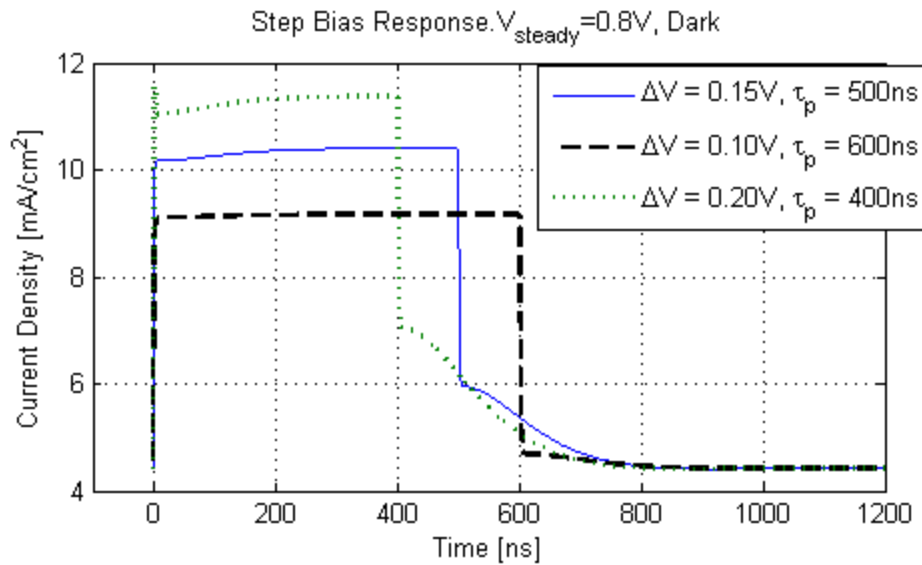
Figure 4.18   Current transients for small *ΔV* and larger pulse widths.

The current overshoot observed for a strong pulse signal, as in Figure 4.19 below, can be explained by the storage charges. These excess carriers near the junction will be swept into the other side of the junction by the strong electric field in the depletion region. Hence a large reverse current will flow temporarily.
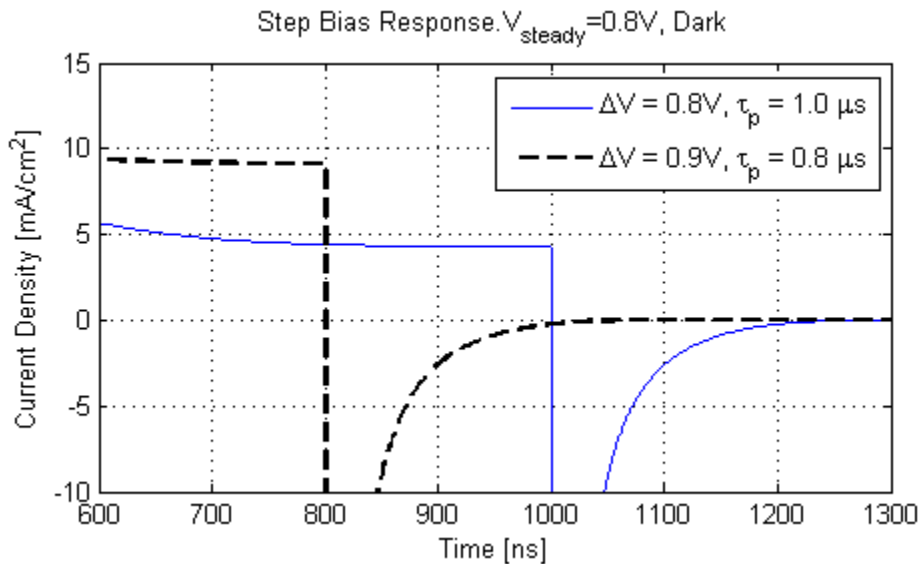

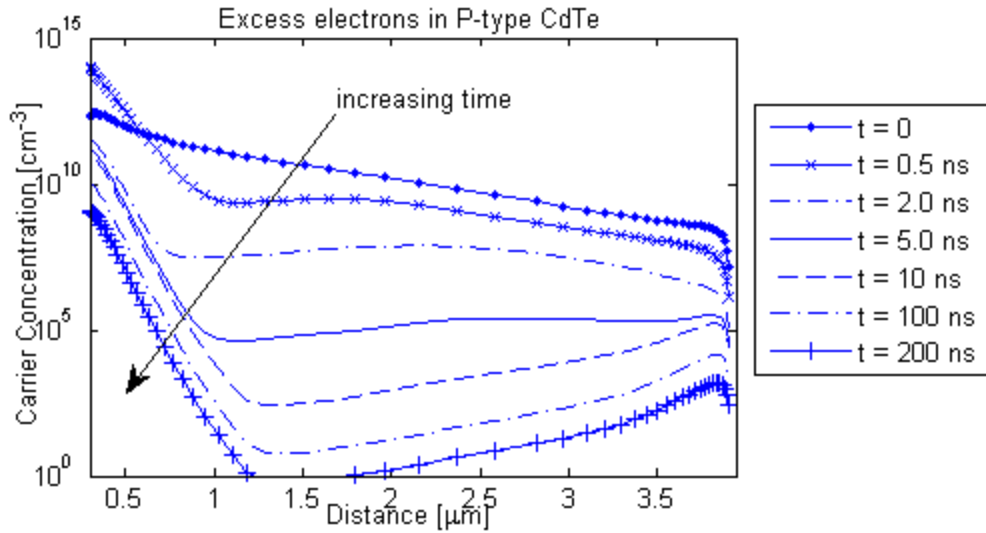Figure 4.19   Reverse recovery transient observed for turn-off.

Figure 4.20   Effects of a step turn-off transient on minority carriers in P-type CdTe.

Figure 4.20 shows the excess minority carriers drifting back to the n side of the junction. As can be seen, the electron concentration below 0.5 μm actually increased in the first 0.5 ns due to the drift in the depletion region.
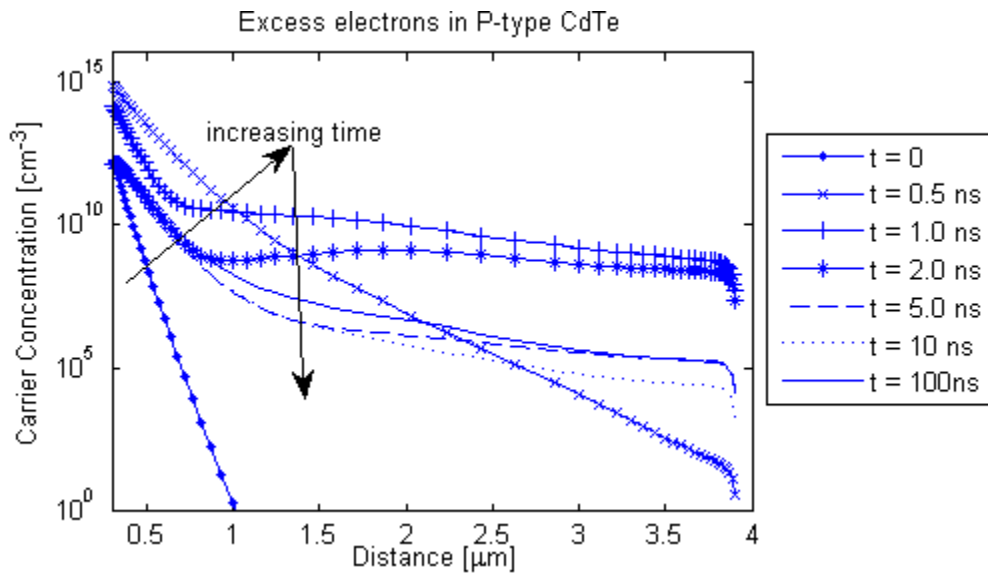

Figure 4.21   Effects of a step turn-on transient on minority carriers in P-type CdTe

As for the turn-on transient, the diffusion process of the minority carriers is

59

produced as depicted in Figure 4.21. Carriers stored in the n side space charge region, diffusing into p side, caused high carrier concentration below 1 μm in the first half nanosecond. These carriers can be further diffused into the entire CdTe layer, as shown for 2 ns, in which case the lower concentration below 1 μm, indicates the number of injected carriers being reduced to a normal level, eventually resulting in the electron distribution of 100 ns.

4.3.2. Photocurrent Transient

Similarly to the step bias response, a variety step functions of illumination have been applied to the standard solar cell under short circuit conditions, so that the current decay and carriers transients can be analyzed. Shown below are the charging and discharging processes in solar cells due to on and off illumination. The natural decay of current has been reproduced in Figure 4.23.
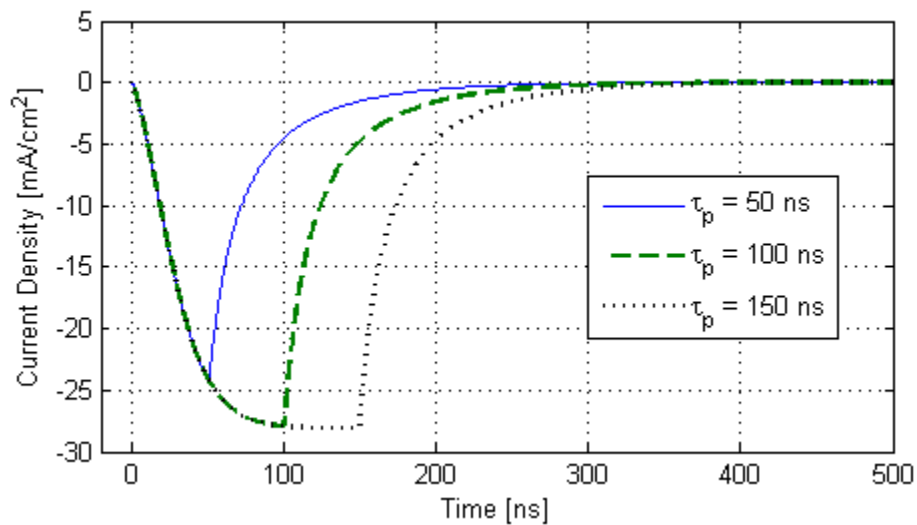

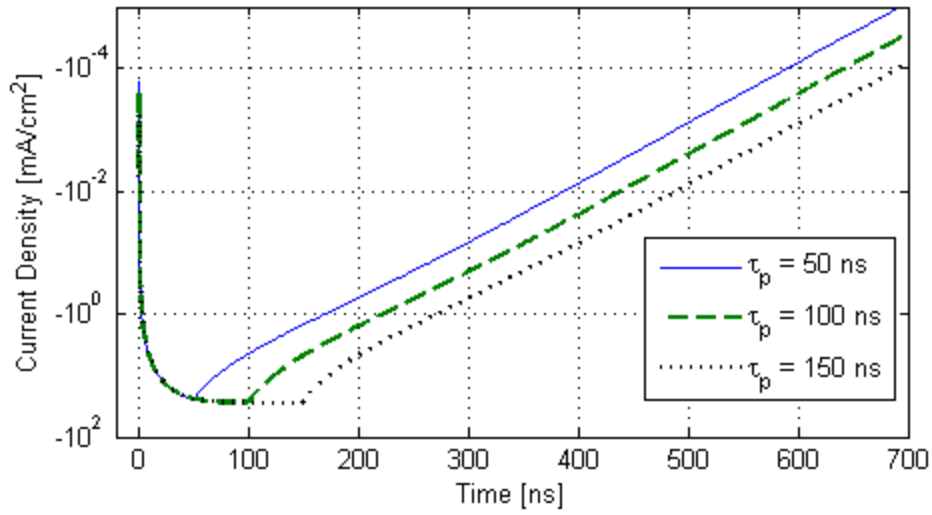Figure 4.22   Photocurrent transients.

Figure 4.23   Exponential decay of photocurrents.

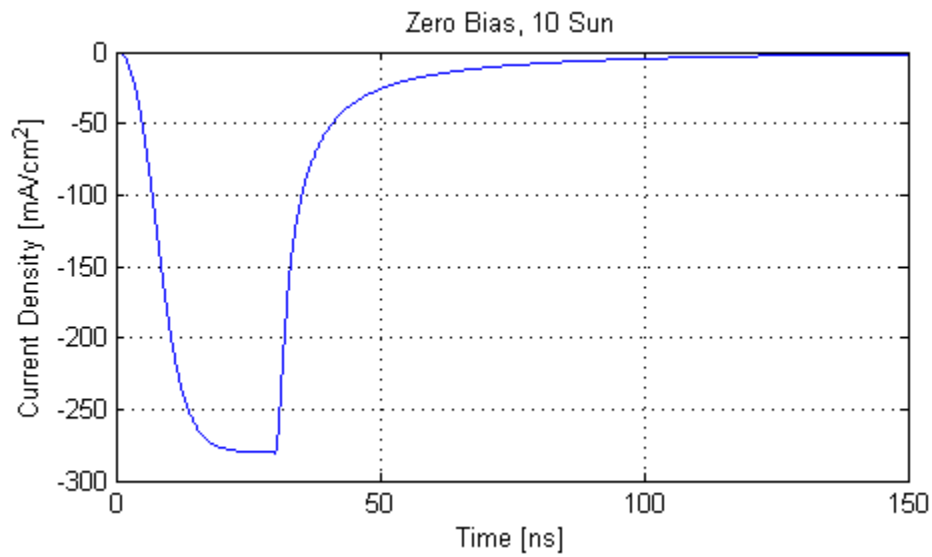Figure 4.24   Current transient under 10 Sun illumination with 30 ns pulse width.

A ten Sun concentrated AM1.5G spectrum lasting 30 nanoseconds, was tested for a clearer view on the majority carrier transients on P-type CdTe. Figure 4.25 shows the process of holes being optically generated and drifting from the depletion region. The black dash line represents the generated holes density within the first 0.01 ns, which

61

matched perfectly with the carriers distribution at 0.01 ns, except the carriers drifted due to strong electric field below 0.4 μm. It is clear that the hole concentration near junction increased to the magnitude of the 30ns distribution, which can be seen as steady state values here, within 0.5 ns.
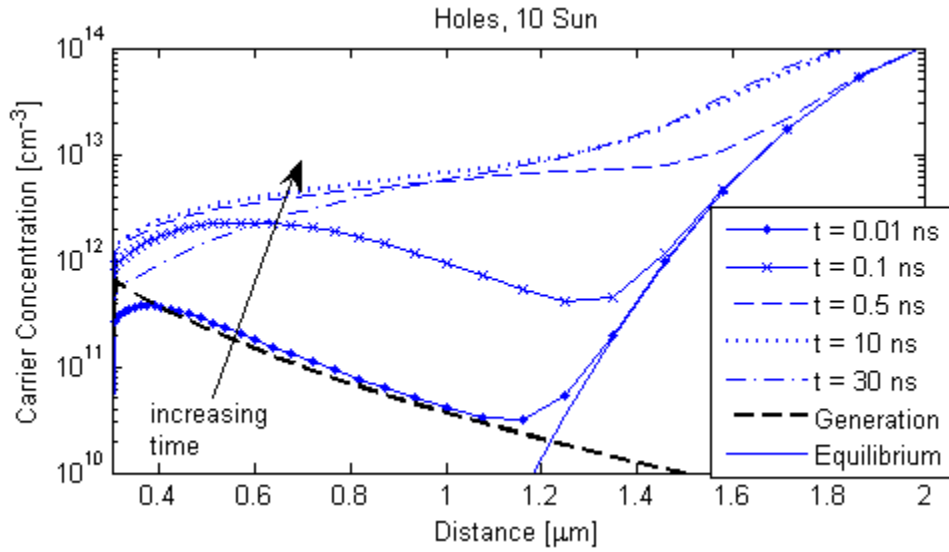

Figure 4.25   Majority carriers' transient near junction in P-type CdTe.
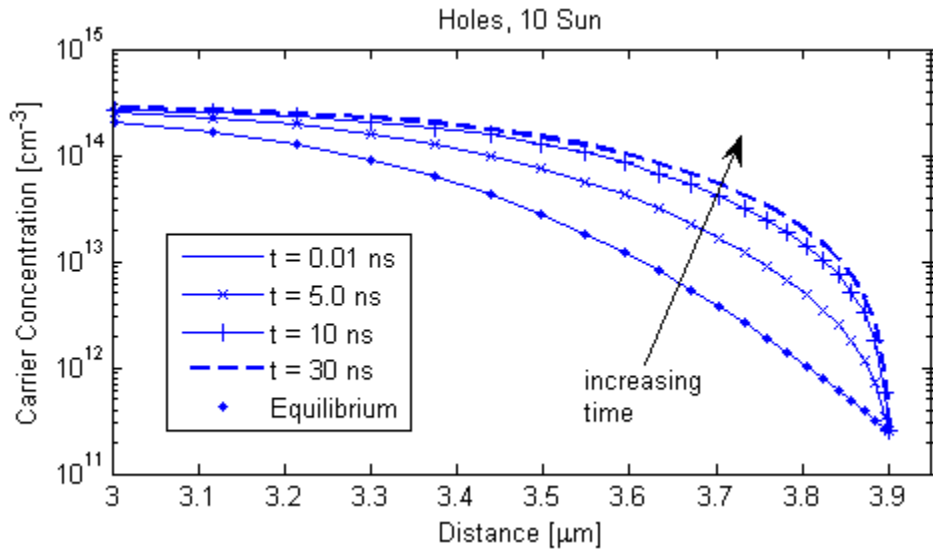
Figure 4.26   Majority carriers' transient near contact in P-type CdTe.

While at the contact region, where optical generation rate can be neglected, it took at least 10 ns for the carrier density to get close to the steady-state value, as illustrated in Figure 4.26; this can also be seen as the carriers generated at the deletion region got drifting to the contact, as current flows.

Figure 4.27   Turn-off transient of majority carriers near junction in P-type CdTe.

Figure 4.28   Turn-off transient of majority carriers near contact in P-type CdTe.

As for the turn-off transient after 30ns in Figure 4.24, the reverse processes of the

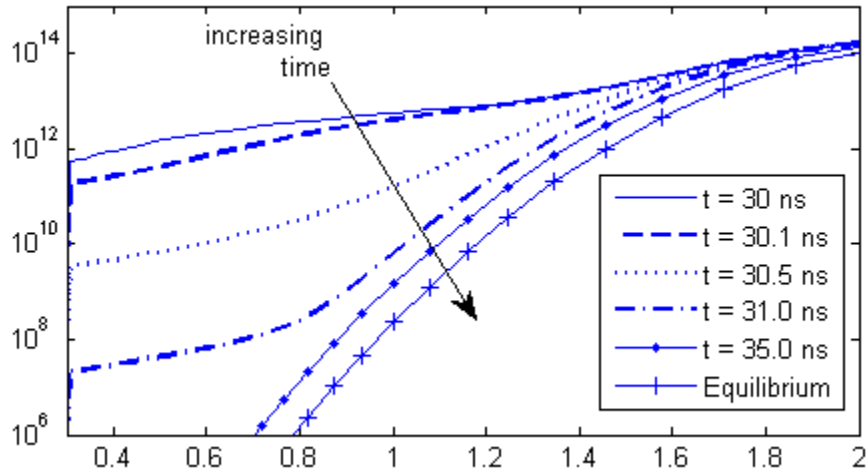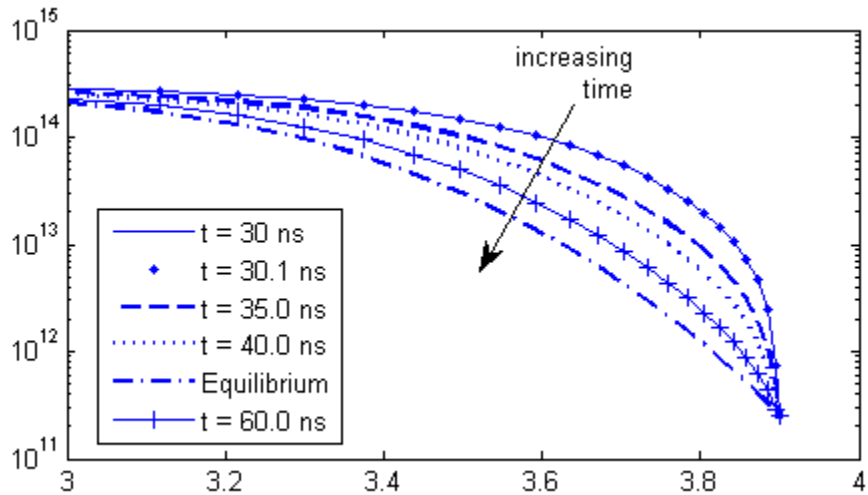turn-on transient were reproduced: the majority carriers near junction drifted away from the depletion region within 5 nanoseconds, while majority carriers at the contact region returned to equilibrium value with at least 30 nanoseconds after the turn-off, as shown above in Figure 4.27 and 4.28. For a more clear view of the drift of holes under illumination, a 10 sun illumination was applied to the device for 0.1 ns, resulting in the following plot.
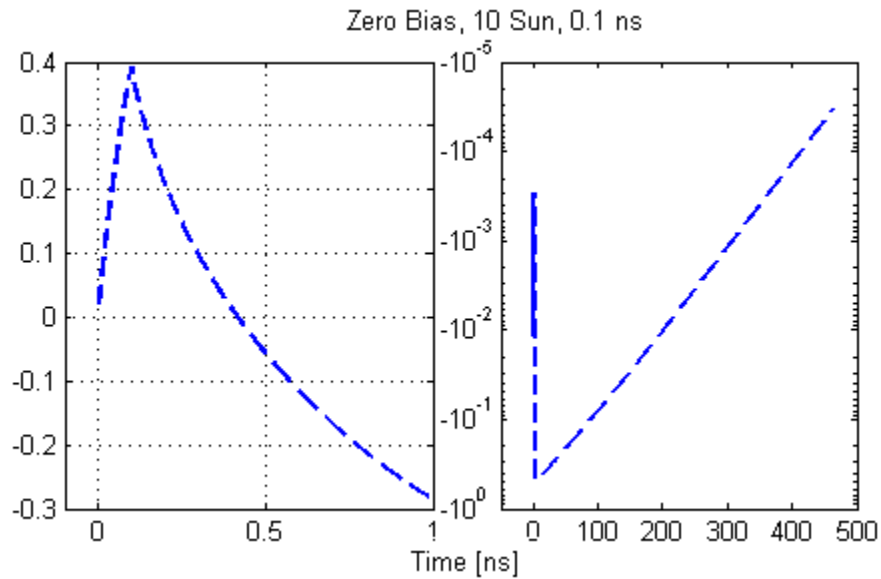
Figure 4.29   Transient of photoluminescence current for a short light pulse.

The positive current in the first 0.1 ns depicted in the left panel of the above graph, was due to the immediate collection of photo-generated holes at the N-type front contact and carrier separation caused by the TiO/CdS heterojunction. The negative current after the turn-off of the illumination is the collection of excess holes at the back P-type contact, which is usually called light current at steady state. Due to the configuration of the solar cell, it may take some time for the holes to travel through the entire device and get

64

collected at the back contact, thus the decay process of the light current took hundreds of nanoseconds, as shown in the left panel of Figure 4.29.

As shown in the excess carrier distribution picture below, the light signal had been transferred into electric signal in terms of carriers movement. Photo generation had been captured well at the first 0.1 ns, while the movement of concentration peaks indicated the drift of carriers within the first nanosecond after the shutdown of illuminations. Also the reduction in carrier velocity was observed, as the displacement of concentration peaks shrinks between 0.1 – 0.4 ns and 0.4 – 1 ns time interval, due to the deeper position in the P-type layer, where electric field was significantly weaker than the junction area.
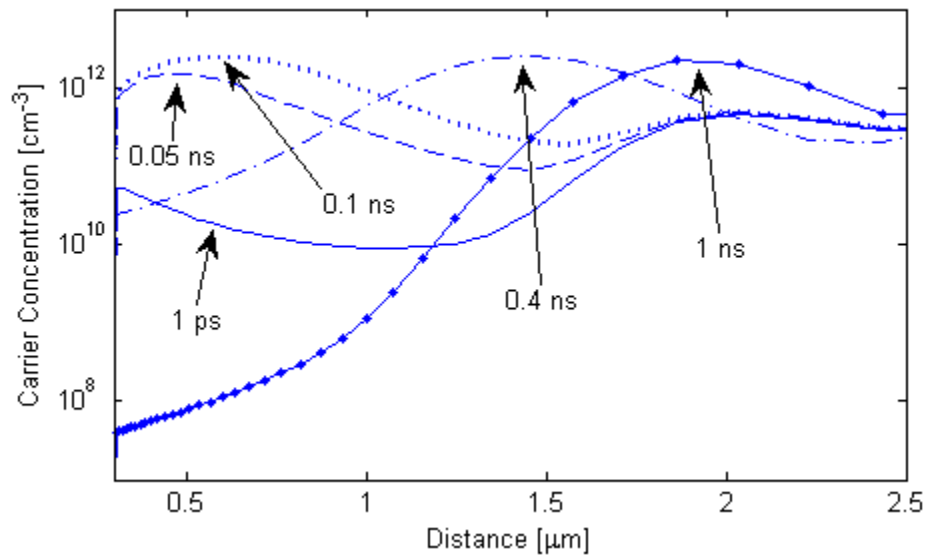

Figure 4.30   Transient of excess holes for a short light pulse.

Chapter 5   CONCLUSIONS AND FUTURE WORK

This chapter summarizes the key features of this thesis project and its results, followed by the plan for future research into the role of the defects in CdTe solar cells.

5.1.   Conclusions

To conclude, a drift – diffusion model has been developed from scratch to simulate the steady state and transient operation of CdS/CdTe solar cells. The self-consistent solutions of potential and carrier distributions are obtained by solving the coupled Poissons' equation and the continuity equations. The configuration of the solar cell is a SnO/CdS/CdTe heterostructure, with an n^+-n^+-p doping profile. The effect of Schottky contact was observed in both dark current and light current simulations. This simulator has been tested for solar cells under dark, and compared to the dark current obtained from other commercial tools with acceptable differences. The conversion efficiency of the device changes with the absorber's thickness due to its ability to capture long wavelength photons but the efficiency starts decreasing after a critical length, due to the loss of uncollected carriers. The capability of modeling the device at low temperature has been certified for temperatures down to 220K. High temperature degradation effect on the device performance was also shown clearly via the simulations presented. The step function bias turn-on characteristics and the effects of storage charges on the turn-off transient, usually called current overshoot, has been reproduced by this solver. The charging and discharging processes caused by illumination were also simulated. Natural decay of photocurrent has been generated. The mechanisms behind these characteristics have been analyzed with the corresponding carrier transients generated by this very

simulator.

5.2.   Future Work

The simulations presented here have been done on a standard SnO/CdS/CdTe abrupt heterojunction solar cell, but the code is capable of modeling graded heterojunctions constructed with other materials. Photon recycling has not been implemented in the current version of code. For complete simulations of Photoluminescence, the absorption of regenerated photons will be implemented in the next version of the code.
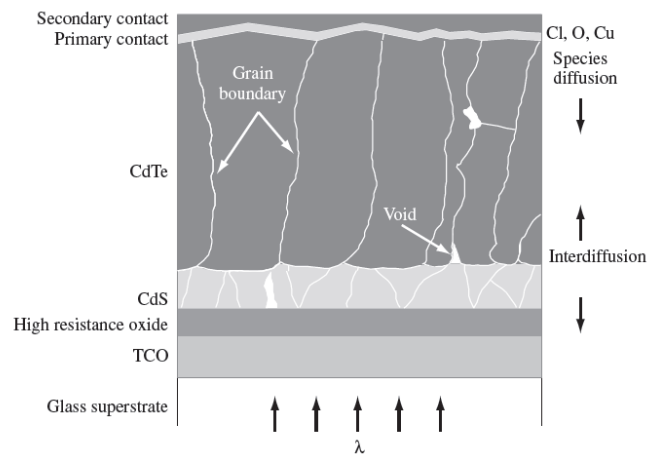
Figure 5.1   The polycrystalline nature of the CdS and CdTe layers are indicated schematically and are not to scale.

Many of the physical properties of crystalline solids depend on the presence of native or foreign point defects and grain boundaries (see Figure 5.1). In pure compound crystals the native defects are atoms missing from lattice sites where, according to the crystal structure, atoms should be (vacancies); atoms present at sites where atoms should not be (interstitials); and atoms occupying sites normally occupied by other atoms (misplaced atoms). In addition, there may be defects in the electronic structure: quasi-free

67

electrons in the conduction band or electrons missing from the valence band (holes). In impure or doped crystals there are also defects involving the foreign atoms. These may occupy normal lattice sites (substitutional foreign atoms) or interstitial sites (interstitial foreign atoms). In elemental crystals similar point defects occur, only misplaced atoms are missing.
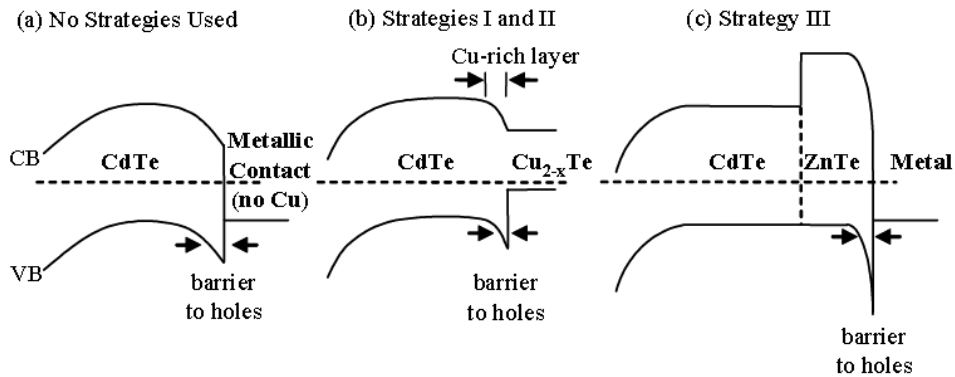

Figure 5.2   Schematic drawing of the band diagram for CdS/CdTe solar cells using different back contact strategies. (a) No strategies used. (b) Strategies I and II, to use an etchant and to dope the back. (Strategy III, to use a material with matching valence band.

Also, the performance of CdTe solar cells strongly relies on the formation of a low-barrier back contact (see Figure 5.2). This usually involves including Cu as a key element in the contacting process. The back-contact behavior and open-circuit voltage (V_{oc}) improve with the application of an optimal amount of Cu during the process. Unfortunately, rapid diffusion of Cu from the back contact toward the main junction is believed to contribute to degradation observed in long-term stability studies. Cu can form both deep interstitial donors Cu_i and substitutional acceptors Cu_{cd} in CdTe. Cu can also migrate along grain boundaries toward the main junction. Thus, while modest amounts of Cu enhance cell performance, excessive amounts degrade device quality and reduce performance. Cu increases the acceptor density in CdTe, however, Cu also forms defects

that lower the lifetime, and hence reduce open circuit voltage V_{oc} and the fill factor (FF). The presence of Cu in the CdS layers is responsible for the crossover and Anomalous QE effects.

REFERENCES

[1]   G. W. Crabtree and N. S. Lewis, "Solar energy conversion," *Physics Today,* vol. 60, pp. 37-42, 2007.

[2]   D. Chapin, C. Fuller, and G. Pearson, "A New Silicon p‑n Junction Photocell for Converting Solar Radiation into Electrical Power," *Journal of Applied Physics,* vol. 25, pp. 676-677, 1954.

[3]   M. A. Green, K. Emery, Y. Hishikawa, W. Warta, and E. D. Dunlop, "Solar cell efficiency tables (version 39)," *Progress in Photovoltaics: Research and Applications,* vol. 20, pp. 12-20, 2012.

[4]   W. Shockley and H. J. Queisser, "Detailed balance limit of efficiency of p‑n junction solar cells," *Journal of Applied Physics,* vol. 32, pp. 510-519, 1961.

[5]   T. Chu, S. S. Chu, C. Ferekides, C. Wu, J. Britt, and C. Wang, "13.4% efficient thin‑film CdS/CdTe solar cells," *Journal of applied physics,* vol. 70, pp. 7608-7612, 1991.

[6]   T. Chu, S. S. Chu, J. Britt, C. Ferekides, C. Wang, C. Wu*, et al.*, "14.6% efficient thin-film cadmium telluride heterojunction solar cells," *Electron Device Letters, IEEE,* vol. 13, pp. 303-304, 1992.

[7]   J. Britt and C. Ferekides, "Thin‑film CdS/CdTe solar cell with 15.8% efficiency," *Applied Physics Letters,* vol. 62, pp. 2851-2852, 1993.

[8]   J. Montgomery. (2013, 02/23/2013). *Solar Cell Efficiency Round-Up: Thin Film Closing the Gap with Silicon*. Available: http://www.renewableenergyworld.com/rea/news/article/2013/01/solar-cell-efficiency-round-up-thin-film-is-closing-the-gap-with-silicon

[9]   I. First Solar. (2012, 02/23/2013). *FIRST SOLAR SETS ANOTHER WORLD RECORD FOR CDTE SOLAR PV EFFICIENCY*. Available: http://investor.firstsolar.com/releasedetail.cfm?releaseid=639463

[10]   D. Vasileska, S. M. Goodnick, and G. Klimeck, *Computational Electronics: Semiclassical and Quantum Device Modeling and Simulation*: CRC Press/Taylor & Francis Group, 2010.

[11]   X. Aymerich-Humet, F. Serra-Mestres, and J. Millán, "An analytical approximation for the Fermi-Dirac integral F32(η)," *Solid-State Electronics,* vol. 24, pp. 981-982, 1981.

[12] A. De Mari, "An accurate numerical steady-state one-dimensional solution of the P-N junction," *Solid-State Electronics,* vol. 11, pp. 33-58, 1968.

[13] M. S. Lundstrom and R. J. Schuelke, "Modeling semiconductor heterojunctions in equilibrium," *Solid-State Electronics,* vol. 25, pp. 683-691, 1982.

[14] S. Selberherr, *Analysis and simulation of semiconductor devices*: Springer-Verlag New York, 1984.

[15] D. Scharfetter and H. K. Gummel, "Large-signal analysis of a silicon read diode oscillator," *Electron Devices, IEEE Transactions on,* vol. 16, pp. 64-77, 1969.

[16] P. A. Markowich, C. A. Ringhofer, and C. Schmeiser, *Semiconductor equations* vol. 19: Springer-Verlag Wien, 1990.

[17] H. Gummel, "A self-consistent iterative scheme for one-dimensional steady state transistor calculations," *Electron Devices, IEEE Transactions on,* vol. 11, pp. 455-465, 1964.

[18] J. E. Sutherland and J. R. Hauser, "A computer analysis of heterojunction and graded composition solar cells," *Electron Devices, IEEE Transactions on,* vol. 24, pp. 363-372, 1977.

[19] M. S. Lundstrom and R. J. Schuelke, "Numerical analysis of heterostructure semiconductor devices," *Electron Devices, IEEE Transactions on,* vol. 30, pp. 1151-1159, 1983.

[20] K. Tomizawa, *Numerical simulation of submicron semiconductor devices*: Artech House Boston, 1993.

[21] K. E. Atkinson, *An introduction to numerical analysis*: John Wiley & Sons, 2008.

[22] J. Bunch and J. Hopcroft, "Triangular factorization and inversion by fast matrix multiplication," *Mathematics of Computation,* vol. 28, pp. 231-236, 1974.

[23] W. Shockley and W. Read Jr, "Statistics of the recombinations of holes and electrons," *Physical Review,* vol. 87, p. 835, 1952.

[24] R. N. Hall, "Electron-Hole Recombination in Germanium," *Physical Review,* vol. 87, pp. 387-387, 1952.

[25] J. Melsheimer and D. Ziegler, "Band gap energy and Urbach tail studies of amorphous, partially crystalline and polycrystalline tin dioxide," *Thin Solid Films,* vol. 129, pp. 35-47, 1985.

[26] J. Nelson, *The physics of solar cells* vol. 57: World Scientific, 2003.

[27] J. Gray, A. Luque, and S. Hegedus, "Handbook of Photovoltaic Science and Engineering," *Luque and S. Hegedus, Eds. West Sussex, England: John Wiley & Sons,* vol. 14, 2003.

[28] J. Parrott, "Radiative recombination and photon recycling in photovoltaic solar cells," *Solar energy materials and solar cells,* vol. 30, pp. 221-231, 1993.

[29] B. G. Streetman and S. Banerjee, *Solid state electronic devices* vol. 2: Prentice-Hall Englewood Cliffs, NJ, 1995.

[30] R. E. Bank, D. J. Rose, and W. Fichtner, "Numerical methods for semiconductor device simulation," *Electron Devices, IEEE Transactions on,* vol. 30, pp. 1031-1041, 1983.

[31] U. Desnica, "Doping limits in II–VI compounds—Challenges, problems and solutions," *Progress in crystal growth and characterization of materials,* vol. 36, pp. 291-357, 1998.

[32] Y.-J. Lee and J. L. Gray, "Numerical modeling of polycrystalline CdTe and CIS solar cells," in *Photovoltaic Specialists Conference, 1993., Conference Record of the Twenty Third IEEE*, 1993, pp. 586-591.

[33] N. Amin, K. Sopian, and M. Konagai, "Numerical modeling of CdS/CdTe and CdS/CdTe/ZnTe solar cells as a function of CdTe thickness," *Solar energy materials and solar cells,* vol. 91, pp. 1202-1208, 2007.

[34] V. Plotnikov, X. Liu, N. Paudel, D. Kwon, K. Wieland, and A. Compaan, "Thin-film CdTe cells: reducing the CdTe," *Thin Solid Films,* vol. 519, pp. 7134-7137, 2011.

[35] L. Kosyachenko and E. Grushko, "Open-circuit voltage, fill factor, and efficiency of a CdS/CdTe solar cell," *Semiconductors,* vol. 44, pp. 1375-1382, 2010.

[36] S. S. Hegedus and B. E. McCandless, "CdTe contacts for CdTe/CdS solar cells: effect of Cu thickness, surface preparation and recontacting on device performance and stability," *Solar Energy Materials and Solar Cells,* vol. 88, pp. 75-95, 6/15/ 2005.

[37] D. Oman, K. Dugan, J. Killian, V. Ceekala, C. Ferekides, and D. Morel, "Device performance characterization and junction mechanisms in CdTe/CdS solar cells," *Solar energy materials and solar cells,* vol. 58, pp. 361-373, 1999.